2006

Improving the stability of amorphous silicon solar cells by chemical annealing

Nanlin Wang
Iowa State University

Improving the stability of amorphous silicon solar cells by chemical annealing

by

Nanlin Wang

A dissertation submitted to the graduate faculty

in partial fulfillment of the requirements for the degree of

DOCTOR OF PHILOSOPHY

Major: Electrical Engineering

Program of Study Committee:
Vikram Dalal, Major Professor
Rana Biswas
Mani Mina
Joseph Shinar
Gary Tuttle

Iowa State University

Ames, Iowa

2006

Graduate College
Iowa State University

This is to certify that the doctoral dissertation of

Nanlin Wang

has met the dissertation requirements of Iowa State University

Signature was redacted for privacy.

Major Professor

Signature was redacted for privacy.

For the Major Program

TABLE OF CONTENTS

ABSTRACT

Amorphous silicon solar cells have been extensively used for many years due to the low cost, easy fabrication and special properties. However, it is found that the properties of a-Si:H solar cells degrade upon light illumination, and this limits the application of a-Si:H solar cells and brings the stability concern. Recently, it has been shown that this instability is correlated with the presence of multiple bonded Si-H bonds (i.e., SiH_2), and a technique, namely chemical annealing, was suggested to improve the stability of a-Si:H. Although a number of results have been reported to improve the stability of a-Si:H films based on chemical annealing technique, no chemical annealed devices with good quality were reported.

In this work, chemical annealed a-Si:H films and devices, and non chemical annealed films and devices were produced in a remote, low pressure ECR plasma enhanced CVD, and systematic experiments were carried out to study the role of chemical annealing in enhancing the stability of a-Si:H solar cells.

It is found that the structure of the films grown using chemical annealing technique depended critically upon whether the annealing was done with hydrogen or plasma. When the annealing was done in hydrogen plasma, the films remained amorphous; in contrast, when in helium plasma, and the annealing time is equal or more than 20 seconds, the films became crystalline. These unusual results show that it is not necessary to have a high hydrogen dilution to obtain nanocrystalline films, and contradict the generally accepted assumption that high hydrogen dilutions are needed to crystallize the amorphous films based on the reactive etching of H ions. Instead, it might be the case that not only the reactive

etching effect from the H ions, but also the ion bombardment play a role in crystallizing the amorphous films.

Comparable helium plasma annealed a-Si films and non helium plasma annealed a-Si films were produced. Upon light soaking, the chemical annealed films show a much lower degradation in photoconductivity than that of non chemical annealed films. Comparable helium plasma annealed a-Si solar cells and non helium plasma annealed a-Si solar cells were prepared as well. Upon light soaking, the degradation in the most sensitive device factor, the fill factor, showed that chemical annealed devices possess a much better stability than non chemical annealed devices. FTIR data of chemical annealed films provide a much less SiH_2 bond content than that of non chemical annealed films. Clearly, it indicates that chemical annealing technique leads to significant improvement in the stability of both films and devices in a-Si:H by reducing the SiH_2 bond density inside.

Similar results happened in hydrogen plasma annealed films and devices. Comparable hydrogen plasma annealed films and non annealed films; comparable chemical annealed devices and non chemical annealed devices could be produced as well. Hydrogen plasma annealed films performed lower degradation in photoconductivity than non annealed films. Chemical annealed devices showed a significantly less degradation in fill factor than non annealed devices. FTIR data demonstrated that the stability of a-Si:H was closely related to the SiH_2 bond content and the chemical annealing technique did reduce the SiH_2 bond intensity

CHAPTER 1 INTRODUCTIONS

1.1 Research Motivation

Hydrogenated amorphous slicon (a-Si:H) is widely used for a number of solid state electronic devices, such as solar cells, solid state photosensors, thin film transistor for liquid crystal displays, photoreceptors, and image pick-up tubes [1]. The extensive applications of a-Si:H origin from its several unique features: (1) it has a very high optical absorption coefficient ($>10^5$ cm^{-1}) over the majority of visible spectrum, making extremely thin film device possible; (2) a simple low temperature deposition process is applicable; (3) the optical bandgap of ~1.7eV lies near the energy at which high solar energy conversion efficiencies are expected; (4) the raw materials is abundant; (5) the materials is easy to dope both p-type and n-type using boron or phosphorous respectively; (6) the electronic properties of electrons and holes are adequate for many device applications.

Although the a-Si provides such unique features, one serious problem associated with a-Si limits its application. This is its stability. Known as Staebler-Wronski (S-W) effect [2], the performance of a-Si:H solar cells and imagers degrades upon exposure to light. This effect can involve very large changes in photoconductivity, and in defect densities, which has strong implications for the technical applications of a-Si:H.

Intensive studies have been carried out to improve the stability of a-Si:H, which includes the development of new deposition techniques and new structures for the devices. Among them, a technique called chemical annealing process is utilized to improve the stability of a-Si:H. Recently, it has been shown that the instability of a-Si:H is correlated with the presence of multiply bonded Si-H bonds (i.e. SiH_2). Chemical annealing relies on the

principle that by subjecting a thin a-Si:H film to ion bombardment, one can reorder its structure and thereby reduce the SiH_2 type bonds, leading to better stability. The technique consists in growing a thin film, typically 15-30 ′, and then subjecting it to bombardment from plasma, and then repeating the cycle. Both inert and reactive gas ions have been used for the annealing cycle. Although a number of results have been reported to improve the stability of a-Si:H films based on chemical annealing technique, no chemical annealed devices with good quality were reported.

In this study, chemical annealing process is utilized to study if it improves the stability of a-Si:H solar cells and materials. Systematic experiments will be designed to study the effect of chemical annealing on the properties of the a-Si films and solar cell devices.

1.2 Fundamentals of Solar Cells

Consider the pn junction shown in Fig. 1.1 with a resistive load. Even there is no bias applied, an electric field exists in the depletion region as shown in figure. When it is subjected to photon illumination, electron-hole pairs can be generated in the depletion region that will be swept out and this produces the photocurrent I_L in the reverse-bias direction as shown.

The photocurrent I_L produces a voltage drop across the resistive load which forward biases the pn junction. The forward-bias voltage generates a forward-bias current I_F as indicated in the figure. Therefore, the net pn junction current, in the reverse-bias direction is [3]

$$I = I_L - I_F = I_L - I_S[\exp(\frac{qV}{kT}) - 1] \qquad (1.1)$$

where the ideal diode equation is used and the I_s is the ideal reverse-saturation current of the pn junction diode. As the diode becomes positive biased, the magnitude of the electric field in the depletion region drops, but does not go to zero or change direction.

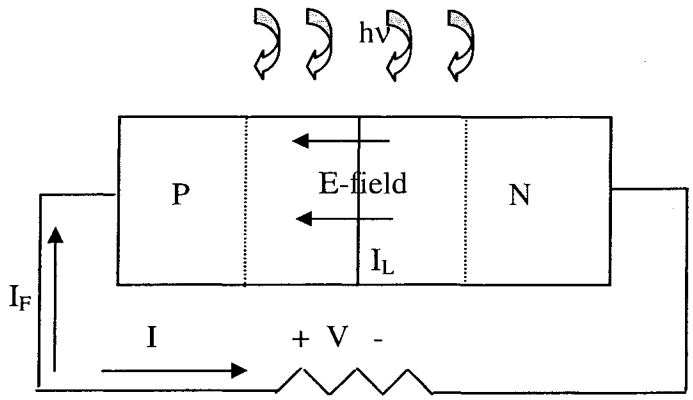

Figure 1.1 A pn junction solar cell with resistive load [3].

In practice, except load resistance R_L, there are two more resistances when a solar cell is under photon illumination. Considering a n^+p junction solar cell with a load resistance R_L illustrated in Fig 1.2 [4], the photogenerated electron has to traverse a surface semiconductor region to reach the nearest finger electrode. All these electron paths in the n-layer surface region to finger electrodes introduce an effective series resistance R_s. A fraction (usually small) of the photogenerated carriers can also flow through the crystal surfaces (edges of the device) or through grain boundaries in polycrystalline devices instead of flowing through the external load R_L. These effects that prevent photogenerated carrier from flowing in the external circuit can be represented by an effective internal shunt or parallel resistance R_p that diverts the photocurrent away from the load R_L.

Fig. 1.3 shows the equivalent circuit of a practical solar cell. The photogenerated process is represented by a constant current generator I_{ph} where the current is proportional to the light intensity. The forward-bias current I_F is represented by a diode with a diode current of I_d.

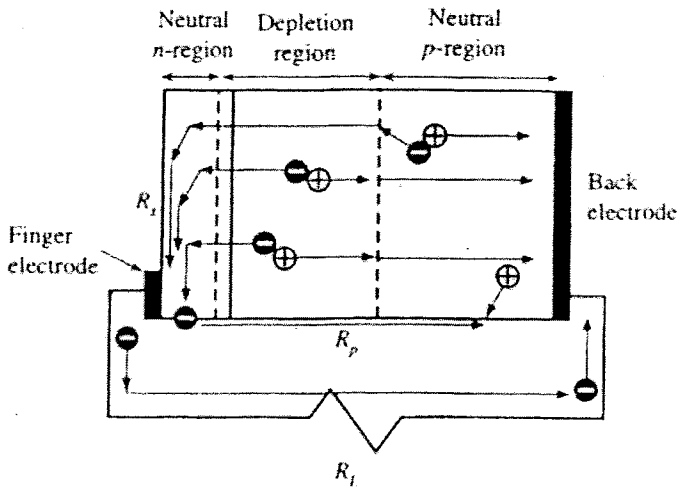

Figure 1.2 Series and shunt resistances in a solar cell [4].

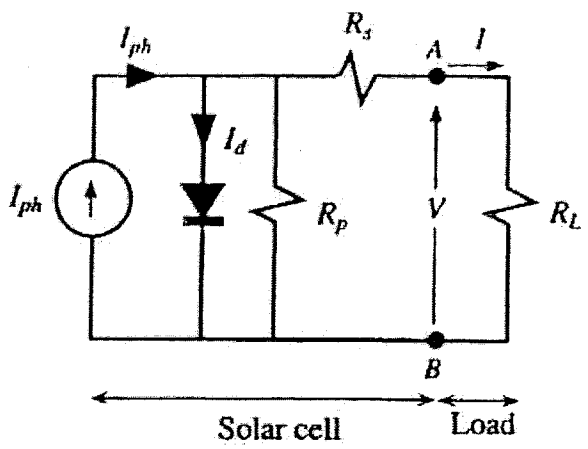

Figure 1.3 Equivalent circuit of a solar cell [4].

The structure of a real device used in this research is shown in Fig. 1.4. The devices are fabricated on rough-polished (not electro-polished) stainless steel substrates. First, the n layer is deposited using H-ECR process. The n layer is about 230-250nm thick and it is an a-

Si:H layer doped with phosphorus. A thick n layer is needed because of the rough substrate. Next, the i2 layer is deposited, for a-Si:H solar cell, using a mixture of hydrogen and silane, or helium and hydrogen and silane. Very small amounts (0.3-0.5ppm) of trimethyl B was added to the i2 layer to act as a compensating dopant against the inevitable oxygen contaminant represent in the reactor. The typical i2 layer thickness is 200nm-300nm. The purpose of the i2 layer is to improve the absorption of the photons. The i2 layer is followed by a i1 buffer layer of graded gap a-(Si,C), which not only provides the bandgap matching between i2 and p layer, but also reduces the B diffusion from p layer. i1 buffer layer is then followed by a thin (20nm) a-(Si,C) p layer. Finally, an ITO contact is deposited on top. The band diagram of a typical a-Si:H solar cell is shown in Figure 1.5.

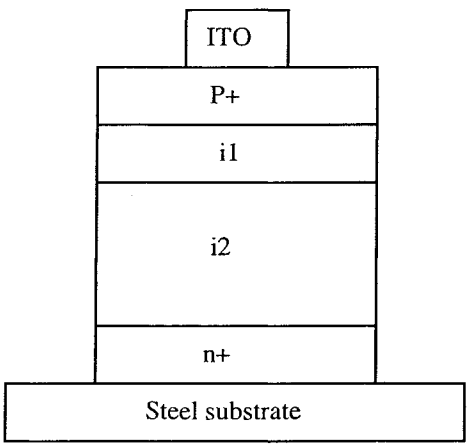

Figure 1.4 Device structure of α-Si:H solar cell.

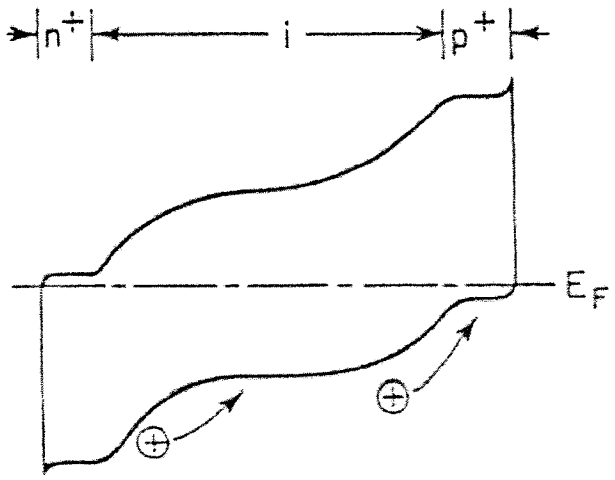

Figure 1.5 Band diagram of a typical a-Si:H solar cell.

1.3 Properties of a-Si:H

Several deposition techniques, such as plasma-enhanced chemical vapor deposition (PE CVD), hot wire-chemical vapor deposition (hot wire CVD) and reactive sputtering, can be employed to produce amorphous silicon. In these processes, hydrogen is either added or released during the deposition. Hydrogenated films containing about 4 to 40 atomic percentage of hydrogen film are generally denoted as a-Si:H.

Unlike the crystallite silicon, a-Si:H has only a order structure in short range. In a perfect crystalline silicon structure, all four covalent bonds of an atom are saturated, and no unpaired spins show up in electron spin resonance (ESR) measurement [5]. But for amorphous, based on continuous random network structure model [6], it shows that the average number of next neighboring atoms is lower than four, so a certain fraction of atoms

is only coordinated with three or less nearest neighbors. A illustration of continuous random network about a-Si:H is shown in Fig. 1.6 [7].

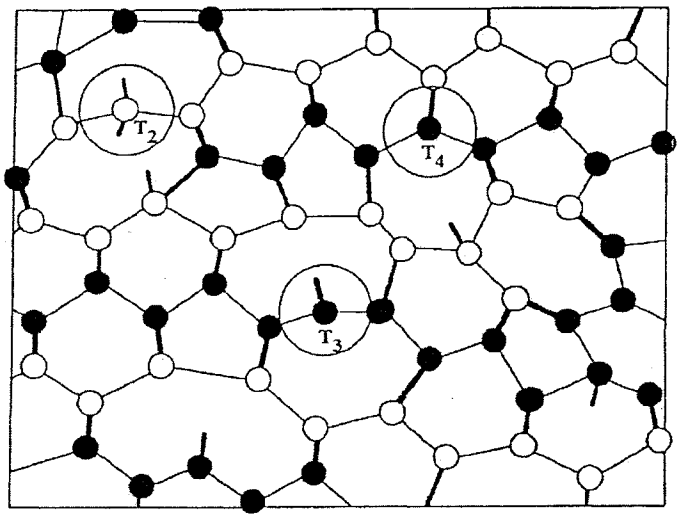

Figure 1.6 Structural atomic model of the covalent bonding in a-Si [7]

In this tetrahedral network model, silicon atoms bond covalently to four neighboring silicon atoms with small deviations of the bonding lengths and angles from those of the crystalline material. Atoms with lower co-ordination occur because they locally release the strain in the disorder structure, which leaves unpaired electrons and is known as dangling bond. These dangling bonds will act as recombination centers and be detrimental to solar cell performance. Besides the dangling bonds, the deviation of the bonding lengths and angles contribute to formation of a continuous energy distribution of density of states as well. In order to decrease the dangling bonds, hydrogen passivation is applied. A hydrogen atom with a single electron can supply an electron and complete an unsaturated covalent bond. This removes the dangling bond level from the forbidden bandgap (passivation) and traps the hydrogen. It was shown in the previous research that the number of dangling bonds is about

10^{20}-10^{22} cm^{-3} in a-Si before being passivated by hydrogen. After the passivation, the number drops to about 10^{15} cm^{-3} [8].

In order to obtain more insight into the electronic properties of amorphous silicon, it is important to determine the distribution of the trap states in the bandgap. Fig.1.7 shows a density of states curve for a undoped a-Si:H film. Since the majority of atoms are still fourfold co-ordinated, the essential features of the crystalline band-structure, the existence of extended valence and conduction band states, are still maintained. The lack of long-range order and distortion of the covalent bonds of fourfold co-ordinated neutral silicon atom in amorphous structure gives rise to a gradual, approximately exponential decrease of the density of states, so called band tails, given by

$$N_{TC} = N_{C0} \exp \frac{E_C - E}{E_{urc}} \qquad (1.2)$$

$$N_{TV} = N_{V0} \exp \frac{E - E_V}{E_{urv}} \qquad (1.3)$$

where N_{TC} and N_{TV} are density of states (DOS) for conduction band tail states and valence band tail states respectively; and E_{urv} and E_{urc} are the characteristic widths of the conduction and valence band tails and called the Urbach energy. For a-Si:H, the typical values of $N_{C0} = N_{V0} = 10^{21}$ to 10^{22} $eV^{-1}cm^{-1}$, E_{urv}= 42-45meV and E_{urc}=26meV [9], which means that valence band tail extends deeper into the gap. Low Urbach energy implies less disorder, which is a very important property of amorphous a-Si:H. It should be noted that a fraction of tail states also originates from silicon atoms with three silicon neighbors and one hydrogen atom in tetrahedral configuration. These additional states from the silicon hydrogen bond change the

optical band-gap, depending on the hydrogen content. The optical gap increases from about 1.5eV for pure amorphous silicon to about 2.0eV when 30 at. % hydrogen is present.

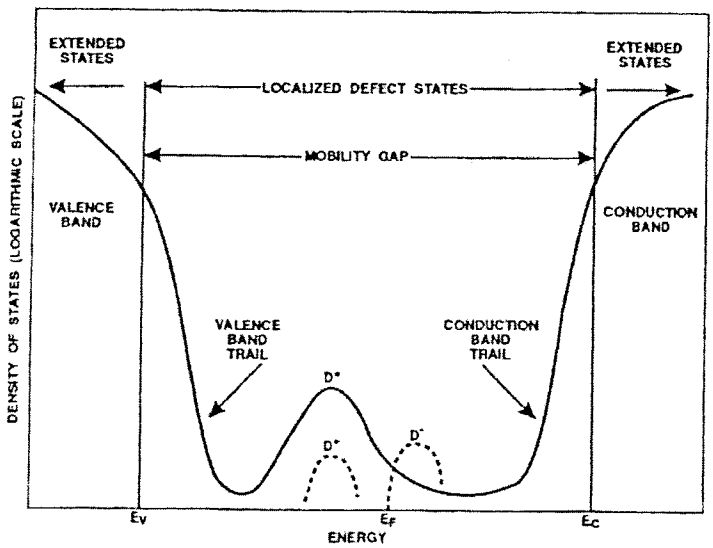

Figure 1.7 Electronic density of states in a-Si:H [7]

Adjacent to the band tail states are several deep-level bands in the lower and upper half of the bandgap, which is considered to be related to dangling bonds of mainly threefold co-ordinated silicon atoms.

Crystalline silicon as an indirect semiconductor has a rather low absorption in the visible spectral range, since only a few of the electronic states near the band edge can take part in the absorption process because of the momentum conservation rule and the participation of phonons. This situation is different for amorphous silicon because the rule of conservation of momentum does not hold and most of the electronic states near the band edges (tail states) are available for optical transitions. Correspondingly, the optical absorption coefficient is much larger than that of crystalline silicon. This is shown in Fig. 1.8 [1].

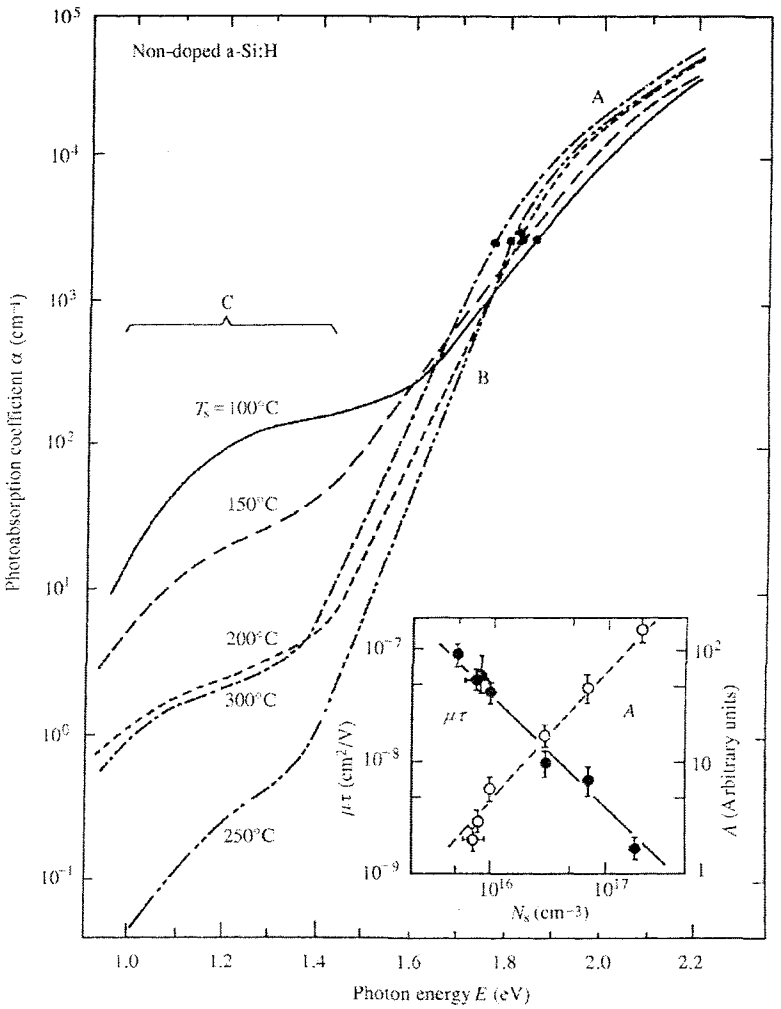

Figure 1.8 Optical absorption coefficient of a-Si:H [1]

Figure 1.8 gives a typical example of the absorption spectrum of non-doped a-Si:H. In this figure, region A is generally termed the "Tauc region", where the spectral form can be approximated by equation 1.4, and is attributed to the optical electron transition between the extended valence band and the conduction band:

$$\alpha\hbar\omega = B(\hbar\omega - E_{tauc})^2 \quad (1.4)$$

where E_{tauc} is termed the optical energy (or Tauc) gap, and is normally used for defining the energy gap of amorphous semiconductors. The typical value for a-Si:H is 1.7 eV. Region B

in Fig. 1.8 is known as the "Urbach region" and has an exponential form given by the following:

$$\alpha = \alpha_0 \exp \frac{h\nu - E_g}{E_{urv}} \qquad (1.5)$$

where E_{urv} is called the Urbach energy. This region can be described in terms of a transition between a band-tail state and an extended band. Furthermore, region C in Fig. 1.8 can be attributed to the mid-gap states absorption. This region has a strong influence on the absorption for low photon energies. Figure 1.8 shows that hydrogen-free amorphous silicon has a significantly larger absorption below the mobility gap of about 1.7 eV for lower photon energies, which is due to the much higher density of trapping states in the gap.

Finally, some properties of device-quality a-Si:H are given here:

(1) Bandgap: 1.7 to 1.8 eV

(2) Urbach energy: 42 to 45 meV

(3) Photoconductivity: 10^{-4} S/cm to 10^{-5} S/cm

(4) Dark conductivity: 10^{-10} S/cm to 10^{-11} S/cm

(5) $\mu\tau$ (mobility-lifetime product) for hole: $\geq 10^{-8}$ cm^2/V

(6) $\mu\tau$ (mobility-lifetime product) for electron: ~ 2×10^{-7} cm^2/V

1.4 Literature review

As mentioned above, hydrogenated amorphous silicon presents a serious problem of metastability. Whereas the original state has a clearly defined conductivity, the metastable state can have a range of conductivity depending on the light exposure.

The physics of instability of an a-Si:H is associated with its non-equilibrium state, and an external disturbance, either thermal or optical, will induce structural changes at the macro- or microscopic levels. Under the illumination of light exposure, electron-hole pairs will be generated. The photo-generated electron-hole pairs combine in the film and release energy, which breaks weak Si-Si and /or Si-H bonds and creates defects, and in turn deteriorates the conductivity of the film. The degradation process can be described by three models: (1) the Trap-to–dangling bond conversion model, first proposed by Adler and quantified by Dalal [10], proposes that both positively correlated dangling bonds (D^0) and negatively correlated charged defect states ($T3^-$ and $T3^+$) exist in the a-Si material. The capture of a charged carrier by an oppositely charged defect state leads to the conversion of this trap state into a positively correlated dangling bond state, thereby leading to an increase in D^0 states and an increase in recombination; (2) Bond breaking-SJT model [10], proposes that the energy released by recombination of an electron-hole pair, leading to breaking of weak Si-Si bonds, thereby creating dangling Si bonds which give rise to increased density of midgap defect states; (3) H Collision model [11] proposes that recombination of photogenerated carriers excites mobile H from Si-H bonds, leaving three fold coordinated Si dangling-bond defects. When two mobile H atoms collide and associate in a metastable two-H complex, the two dangling bonds from which H was emitted also become metastable. Measurements show that during illumination the dangling bond density increases from low starting value of about 10^{16} cm^{-3} up to values of about 10^{17} cm^{-3} [12]. It should be noted that this process is reversible. In 1977, Staebler and Wronski found that both the dark and photo-conductivity of a-Si:H, after being illuminated with band-gap light for a long period of time were reduced, with restoration being achieved by annealing at 180°C [2].

For a-Si:H solar cells, these photo-generated mid-gap defects act as recombination centers, thereby reducing the lifetime of both electrons and holes. These defects also act to reduce the electric field in the middle portion of the i-layer, and this in turn reduce the field-assisted drift length or range and decrease the collection of the carriers in i-layer.

In order to improve the stability of a-Si:H, all kinds of research have been developed, which includes the development of new deposition materials, new fabrication methods, and new structures for the solar cell devices.

Among the new fabrication techniques, remote ECR growth [13, 14], hot wire growth [15], multichamber systems [16] have been reported to improve the stability of a-Si:H solar cells. It is reported by Dalal et al. that the remote ECR process can greatly improve the stability of a-Si:H solar cells compared to the glow discharge techniques [14].

For the new structure design about a-Si:H, Dalal et al. showed that the stability of a-Si:H solar cell with graded i layer bandgap can be greatly improved compared to that of a-Si:H solar cell with constant i layer bandgap [17]. Research also is carried out to improve the stability of a-Si:H solar cells by using of blocking/insulator layers, grading or P^+ multilayered, i/n interface grading, tailoring of the i-layer [18], and tandem type solar cells [19].

Study on the deposition materials has given us valuable results as well. Among them, high Hydrogen dilution [20], He-dilution [21], deuterium dilution [22], and SiF_4 or SiH_2Cl_2 [23] have been employed to improve the stability of a-Si:H.

The light-induced degradation of a-Si:H is shown to be related with hydrogen concentration, especially with Si-H_2 (C_{SiH2})bond density [24]. Studies found that a higher hydrogen content in the a-Si:H causes greater metastable changes [25-27]. It is also found

that the deterioration of film increases with the increase of SiH_2 bond [28]. In recent work, it was shown that after the Si-H_2 content was decreased by either hydrogen dilution or a triode deposition system, the stability of the a-Si:H was improved greatly [29].

According to the growth chemistry of a-Si proposed by Dalal [30], this can be explained by the microvoids introduced by the extra H or SiH_2. If the surface hydrogen is not removed and Si not cross-linked, the bonded Si-H structure gets buried, new material grows around it, and a microvoid forms once the Si-H bond breaks down. The shift in IR signal can arise from H bonded at internal surfaces of voids. The SiH_2 radical introduces the same problem (mirovoid) like extra H does. By combing the SAXS results with infrared measurements, Williamson et al [31] deduced that at the interior surfaces of these microvoids are largely unhydrogenated after degradation, containing at most 4-9 bonded H atoms. Moreover, the presence of microvoids also allows the existence of the SiH_2 polymer chains in the material. These chains are a primary cause of the degradation, since H there is loosely bonded, compared to the random Si-H bond in the bulk, and breaks rather easily upon energetic excitation [32]. The detailed discussion will be provided in the section 2.2, growth chemistry.

In order to eliminate the extra H and get a structure with fewer voids, there are three ways to achieve such goal.

(1) Increasing the temperature of growth. A higher deposition temperature will break the weak Si-H and thus provide a more dense structure. Moreover, at the high temperature, the radicals leading to film growth are more mobile, and hence presumably a better/dense microstructure. However, increasing temperature of growth may result in the breaking of some inevitable weak Si-Si or Si-H bonds, thereby introducing defects.

(2) Using ion bombardment. We can use both reactive species like H or F, and non-reactive ion like He or Ar. The role of H ion is different from role of He ion. H ion is assumed to remove H from the surface by etching (or reaction), enhances radical selectivity by increasing the fraction of silyl (SiH_3) radicals in the growth process. H ions with enough energy (>2-3 ev) can also penetrate the lattice and involve in the subsurface bond reconstruction. He ions can not remove the H (due to non-reactive) and penetrate the surface (due to larger atom size), but serve to impart energy and momentum to the growing surface, which will break the weak Si-H bond and improve the movement of the SiH_3 radicals. It should be noted that an ion bombardment with a low energy is required. High energies lead to defect creation. Based on H_2 dilution or He dilution, H content was found decreased by H ions or He ions, and the stability of the a-Si: H was found improved greatly [28, 21].

(3) Depositing the material at high temperature but provide an in-situ annealing to rebond the weak sites.

The process of eliminating the H is also the process to eliminate the SiH_2 bond. Si-H_2 radical is thought to originate from the contribution of higher-order-silane related radicals like Si_2H_6, SiH_8...and form internal voids. The dissociation energy for silane molecule to produce SiH_3 radical is 8.75 eV, and 9.47eV is for SiH_2 [28]. Impact of electrons with energy above 9.47eV to a silane molecule produces the so-called short life radicals (e.g. SiH_2), which generate higher-order silane-related species by the insertion reaction as follows: $SiH_4+SiH_2 \rightarrow Si_2H_6$, $Si_2H_6+SiH_2 \rightarrow Si_3H_8$... Low pressure and high H dilution prevent formation of these higher radicals.

Recently, a novel technique called "chemical annealing (CA)" or "layer by layer deposition" is introduced to remove the H and improve the stability of a-Si:H. The whole

deposition for CA is composed of many periodic cycles (layers). In each cycle (layer), a layer of thin a-Si:H is followed by a Ar or He or H2 radical (and/or ion) treatment (bombardment). The thickness of each cycle depends on the growth time and the time ratio between the growth and ion treatment, and varies from several tens Å to several nm. In addition to this process, some researchers applied an alternative process, in which the deposition is composed of periodic low hydrogen dilution layer and high hydrogen dilution layer [33, 34]. The high hydrogen dilution layer plays the same role as ion treatment, but the intensity is smaller.

The advantage of CA process is: (1) each growth layer is followed by an immediate ion bombardment; this is supposed to be more efficient to take the extra H away and improve the stability better. (2) It is a very efficient way to tune the bandgap. As we know, the bandgap of a-Si:H increases with the H content. This may be interpreted qualitatively as the partial replacement of Si-Si bonds with Si-H bonds of greater bonding energy [1]. The tunable bandgap of a-Si:H is a very promising alternative for the electronic devices, like tandem solar cells etc. The normal way to change the band gap of a-Si:H and related materials is to introduce germanium or carbon. This alloying increased inhomogeneity in the amorphous network and increased the density of both mid gap state and tail states [35]. But this will not happen to a-Si:H tuned with CA process because the dangling bond is saturate by H.

The fundamental work is represented by the Shimizu group [35-39]. The important results from Shimizu's group can be generalized as:

(1) The optical band gap (Tauc gap) of a-Si:H was varied from 1.5eV-2.0eV by varying deposition time/H ion treatment time in one cycle, as well as substrate temperature

and rf power. The bandgap is found to increase with H content. The materials with low H content showed excellent transport properties and improved stability [35].

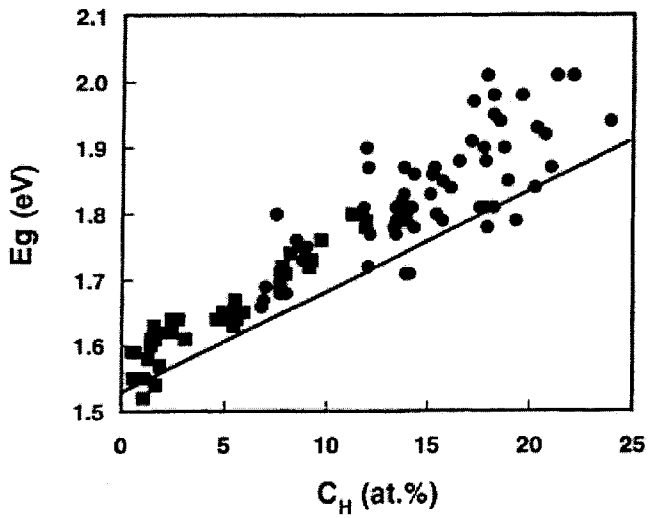

Figure 1.9 Tauc's gap plotted as a function of total hydrogen content for chemical annealing a-Si:H [35]

(2) Not only H ion treatment, but also Ar, He, or Ne radicals/ions can reduce the bandgap of a-Si:H based on chemical annealing. High quality narrow band gap (<1.6eV) a-Si:H with a $\mu\tau$ product of 7×10^{-8} cm^2/V for electrons and 3×10^{-8} cm^2/V for holes were obtained [36].

(3) Stability of p-i-n solar cell based on Ar CA was compared with standard a-Si:H solar cell fabricated from SiH_4 without H_2 dilution. Measurement found that in the beginning the standard solar cell has a higher FF, but after a light soaking of ~700 minutes, the FF of the standard one drops below that of the CA one [37]. However, the FF of CA devices was low, ~55% range, implying high defect density.

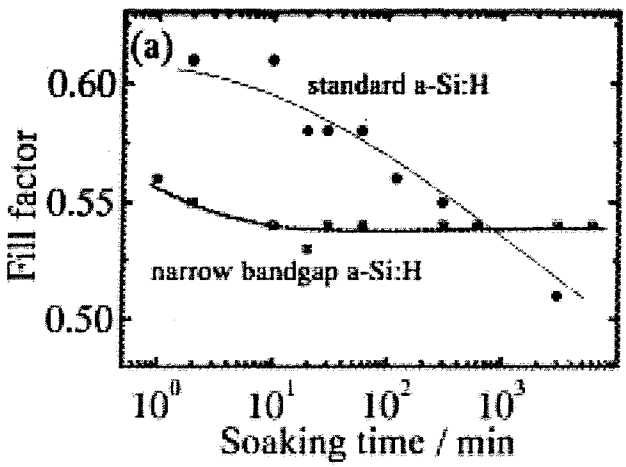

Figure 1.10, FF of the CA solar cell and standard solar cell as a function of light-soaking time [37].

(4) When substrate temperature is higher than 200°C, hydrogen radical flux was found to promote crystallization! While when the addition of Ar ion is introduced into H, the crystallization was partly prevented with the aid of ion-bombardment [38].

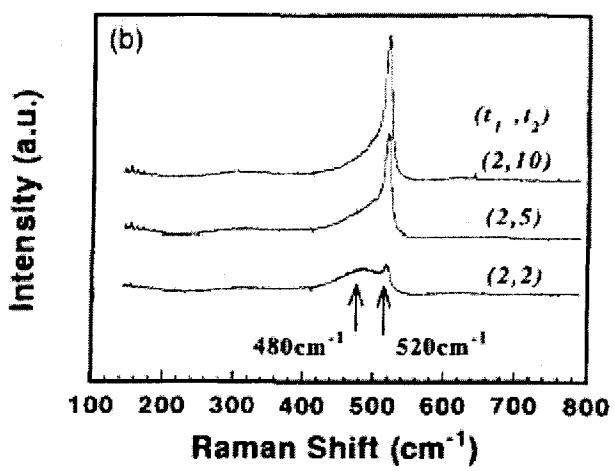

Figure 1.11, Raman spectra for CA films by varying the durations (t1,t2). t1 is the deposition time in seconds and t2 is the annealing time in seconds [38].

The most coinciding demonstration that CA by H plasma significantly improves the microstructure of a-Si was provided by work in Prof. Hirose's group [39]. In Figure 1.12, Raman scattering spectra for a 2 nm-thick a-Si:H film shown that the band intensity due to the wagging mode of SiH_x decreased after the H_2 plasma treatment while the intensity due to the a-Si TO-like phonon increased, which indicates the hydrogen desorption from the hydrogen-rich surface layer during the H_2 plasma treatment.

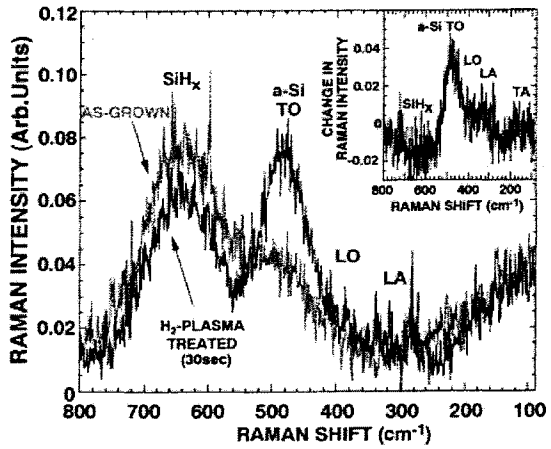

Figure 1.12, Raman scattering spectra for 2nm-thick a-Si:H film before and after H_2 plasma treatment for 30s [39].

1.5 Scope of research

Although systematic studies have been carried out by Shimizu group [35-39], some fundamental questions are still not solved.

First, they reported that by H CA, crystalline tissue can be obtained, and this is not found in inert gas CA, like Ar or He. But the growth mechanism for crystalline tissue, as they mentioned, is still not clear.

Second, although the CA provides improved stability for p-i -n devices, the FF of them are very poor (<55%), which limit the further application of CA devices.

Furthermore, no systematic data (i.e. Urbach energy, subgap absorption, hole $\mu\tau$ product, and SiH_2 bond content) to reveal the relation of chemical annealed a-Si:H samples' properties and stabilities.

In this research, systematic experiments will be designed to study the chemical annealing technique, and see if it can improve the stability of a-Si:H solar cells and materials.

(1) Chemical annealed a-Si:H films prepared by He (plus H) plasma will be made. Previous studies in our group show the necessity for having both H and He or Ar present to prepare good films [40]. The inert He or Ar is supposed to provide heavy ion impinging to break the weak Si-H as well as provide the momentum to the SiH_3 radicals, and the H plays the role to take the broken H bond away. In the meantime, the non chemical annealed a-Si:H films prepared by He (plus H) will be made. The comparisons between CA films and non CA films will be studied. This includes the stability of films in photoconductivity, the SiH_2 bond density, the Urbach energy, the midgap absorption, and the optical band gap etc.

(2) Similarly, chemical annealed a-Si:H films prepared by H plasma and non chemical annealed a-Si:H films by H plasma will be made. And the comparisons between them will be studied as well.

(3) As mentioned above [38, 39], H plasma treatment during chemical annealing can change the microstructure of a-Si:H and convert the amorphous matrix into nanocrystalline one. But the growth mechanism of this crystalline tissue is not clear. Therefore, specific experiments will be deigned to study this question.

(4) Systematic study of devices will be carried out as well. A more stable CA device with good FF is the goal. Both the He (plus H) and H plasmas will be applied.

(5) The stability between CA devices and non-CA devices will be compared. Fundamental electronic properties of the CA and non CA devices, which includes the holes' $\mu\tau$ product, QE, QE ratio, and Urbach energy, will be studied before and after light soaking so as to elucidate the reasons.

CHAPTER 2 SAMPLE PREPARATION

2.1 ECR PECVD system

The deposition system used in this research is electron cyclotron resonance plasma enhanced chemical vapor deposition system (ECR-PECVD) [40]. Figure 2.1 gives a schematic view of this system.

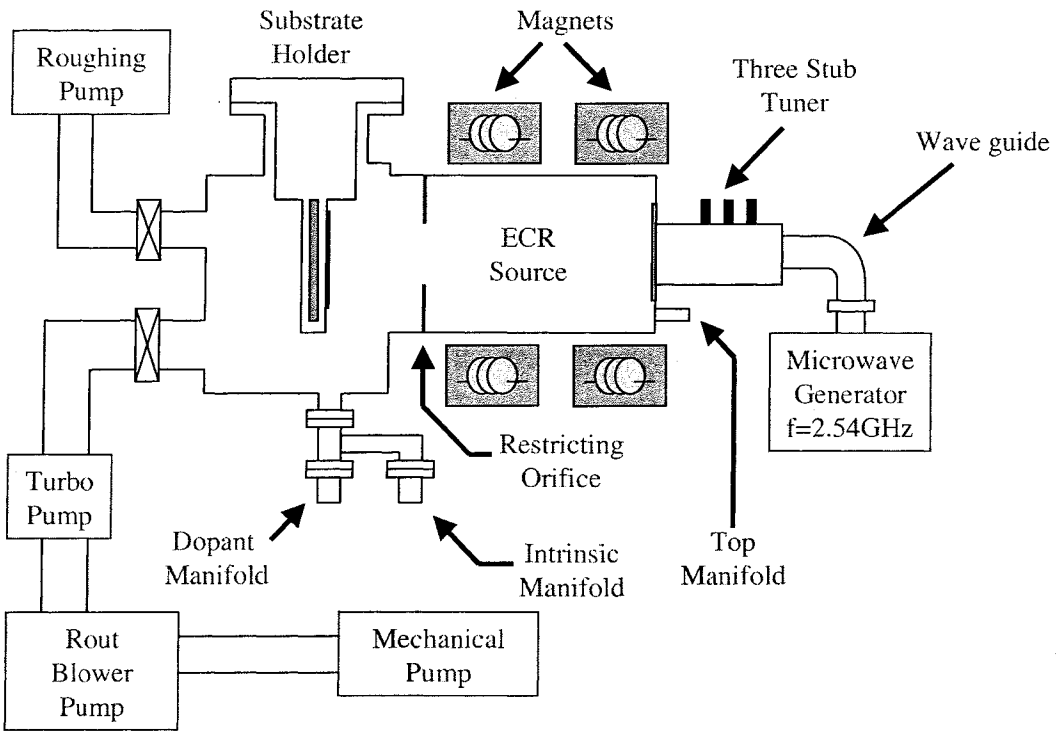

Figure 2.1 Schematic view of ECR-PECVD system [40].

A divergent magnetic field generated by coils surrounding the plasma excitation chamber extracts charged species of the plasma from the excitation chamber into the deposition chamber. The feed-stock gas is introduced in the deposition chamber where the extracted energetic gas species decompose the feed gas (indirect feed-gas decomposition). The excitation chamber operates as a microwave cavity resonator. The magnetic flux density in the excitation chamber is controlled to achieve the circuit motion of electron (ECR) in a

region inside the excitation chamber. The plasma production efficiency is enhanced by satisfying the ECR condition, in which the electron cyclotron frequency (the frequency of the circular motion) is equal to the microwave frequency [41]. More than 70% of the microwave power is absorbed by the plasma. The microwave power required to sustain stable plasma is reduced by one order of magnitude with respect to non-magnetically confined plasma. The frequency of the microwave energy source is 2.45 GHz, which gives a resonance for 874-Gauss magnetic flux density.

Compared to conventional RF glow discharge, ECR PECVD has the following advantages [42]: (1) High ion density at sample location: Electrons absorb energy more efficiently from the microwave source because of the resonance acceleration. Consequently the plasma is much denser than the rf-plasma. The plasma density N_i is $>10^{11}cm^{-3}$, an order of magnitude higher than the RF-plasma. (2) Low ion energy: V_i = 10 – 50eV. The ion bombardment with this energy is extremely important for the growth of the film with good microstructure and other mechanical properties. (3) High degree of gas decomposition and high concentration of excited species and radicals involved in film formation. Disassociation rate as high as nearly 100% can be achieved. This improves the gas utilization and dramatically increases the film growth rate. (4) Low gas pressure: The pressure required to sustain the plasma is much lower, so the danger of gas-phase reactions is minimal. Typical ECR operational pressure is 10^{-4} – 10^{-2} Torr. (5) Easy control of the ion density and ion energy by varying the microwave power and chamber pressure. Additional control over the ion energy can be achieved by substrate biasing. (6) Lower contamination, due to the absence of electrodes. (7)Low energy spread.

2.2 Growth Chemistry

In the ECR PECVD system, there are several reactions near the surface of the substrate:

$$e + SiH_4 \Longleftrightarrow SiH_3 + H^+$$

$$e + SiH_3 \Longleftrightarrow SiH_2 + H^+$$

$$e + SiH_2 \Longleftrightarrow SiH + H^+$$

$$H^+ + SiH_4 \Longleftrightarrow SiH_3 + H_2$$

The dissociation energy for silane molecule to produce SiH_3 radical is 8.75 eV, and 9.47eV is for SiH and SiH_2 [28]. It is believed that SiH_3 is dominant and the most important radicals (90%). SiH_3 has higher surface mobility and low sticking coefficients. If the content of other radicals, such as SiH_4, SiH_2 is high in the plasma, the surface will be rough and many dangling bonds and microvoids will be formed [8].

The standard model of a-Si:H growth is called MGP model. According to Matsuda [43], Perrin [44] and Gallagher [45], it states that the growth of a-Si:H is limited primarily by surface diffusion of a radical such SiH_3. When this radical finds an open site, it bonds, and H is eliminated by breaking of Si-H bonds and subsequent cross-linking of neighboring hydrogen boned to adjacent Si atoms. The schematic diagram of the MGP model is shown in Fig. 2.2. However, a silyl radical bonded to a surface Si is relatively stable; it is almost like a silane molecule. There is no reason for a Si-H bond to break from such a surface-bonded radical at typical growth temperatures, since the bond breaking energy is around 2.5 eV. Therefore, some other mechanism must be responsible for removing this H. The standard model also fails to answer questions such as why bombardment with H ions helps to improve the material, and why low-pressure growth improves the properties of a-(Si,Ge) [30].

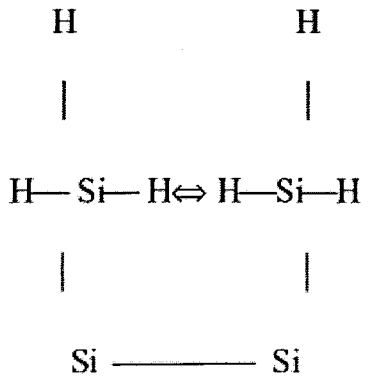

Figure 2.2, Schematic diagram of the growth of Si thin films by elimination of H from neighboring atoms at the surface. Such surface elimination is unlikely [30].

Dalal [30] improved this model. He suggested that the primary consideration which determines the growth of high quality a-Si:H and alloy films is not surface diffusions, but rather the removal of surface hydrogen, and this removal takes place not by reaction between neighboring H bonded to adjacent Si atoms, but rather by extraction of hydrogen by H radicals, and H and inert gas ions. A high H dilution leads to a significant concentration of H ions and radicals impinging on the surface, and these remove bonded H. The H ions also penetrate deeper into the lattice, and remove some more bulk H. The role of inert gas ions, such as Ar and He is to break the surface H bonds, thereby creating a dangling bond, and allowing another silyl radical to insert itself. The inert gas ions do not penetrate deep into the substrate, but H ions do.

According to Dalal's model [46], the growth of a-Si:H is not a simple process. In particular, at least 3 separate steps appear to be necessary for growing good a-Si:H. These steps are: (1) Removal of surface H; (2) Insertion of a SiH_3 radical into the open bond; (3) Removal of inter-atomic H and cross-linking of Si. The whole process is shown in Fig. 2.3.

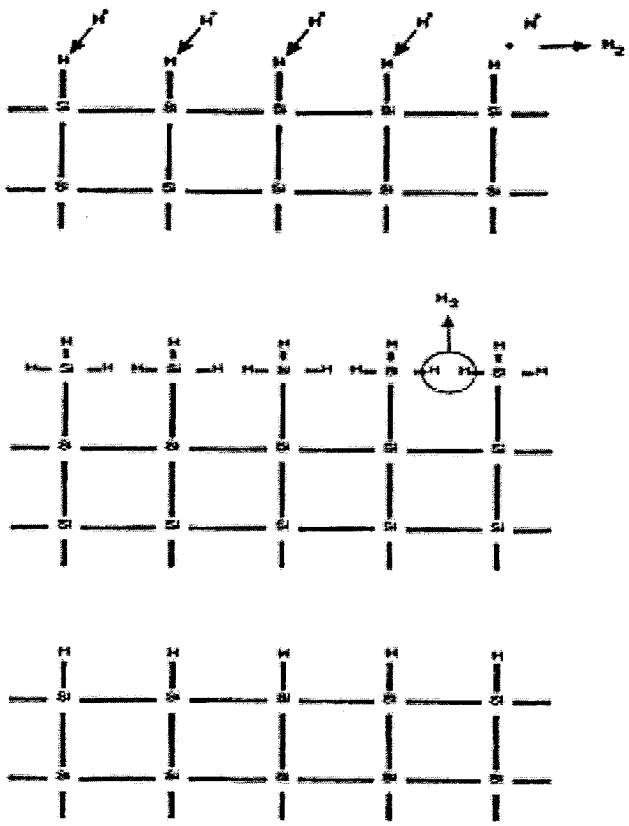

Fig. 2.3 The growth process for a-Si:H films [46].

If the surface hydrogen is not removed and Si not cross-linked, the bonded Si-H structure gets buried, new material grows around it, and a microstructure with a significant void concentration and clustered silicon-hydrogen bonds form in the lattice. As shown in Fig. 2.4 [47], since both SiH_2 and SiH_3 are present in the radicals flux, they both insert in a Si dangling bond at the surface. After insertion, the result is that some bonds are saturated with H, and therefore passive, whereas some are still dangling, and therefore active. Thus, the presence of more than one radical species results in a growth surface with non-uniform bonds. However, when significant excess of H radicals is present, H homogenizes the growing surface by first attaching itself to the surface dangling bond, then the next H atoms

serves to remove the bonded H, and create an active site. And this is true for all the sites; irrespective of which radical (SiH_2 or SH_3) was bonded at the site. Thus, the presence of H serves to homogenize the surface.

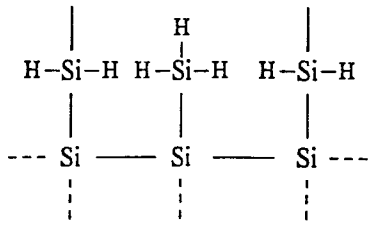

A non-homogeneous surface
in the absence of H dilution

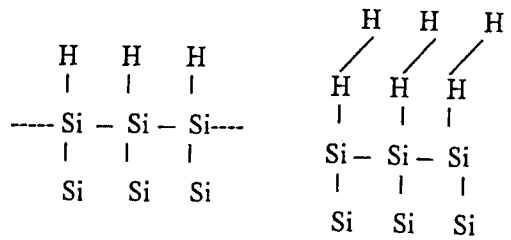

A. Homogenization of surface by H

B. Hydrogen extraction

Figure 2.4 Influence of hydrogen on homogenization of the surface [47]

The effect of SiH_2 on the growth of a-Si:H can be shown in Fig. 2.5. In for a uniform process A with only SiH_3 radicals, first H removes the surface H and leaves open sites, then SiH_3 radicals insert to the open sites, then the neighboring Si-H is broken by ion or thermal energy and atomic H combines (H-H is 435 kJ/mole, Si-H is 300kJ/mole) and removes, and then cross-linking of Si takes place. Finally, a homogenous surface forms with every dangling bond being passivated by H. While in process B, both the SiH_3 and SiH_2 radicals insert to the open sites, after this, some bonds are passivated by H and some are still dangling. In the future growth, the dangling bond can accept other radicals, and the passivated bond cannot if the extra H is not extracted, it will be buried by the material

growing around it. And a microstructure with a significant void concentration and clustered silicon-hydrogen bonds could form in the lattice.

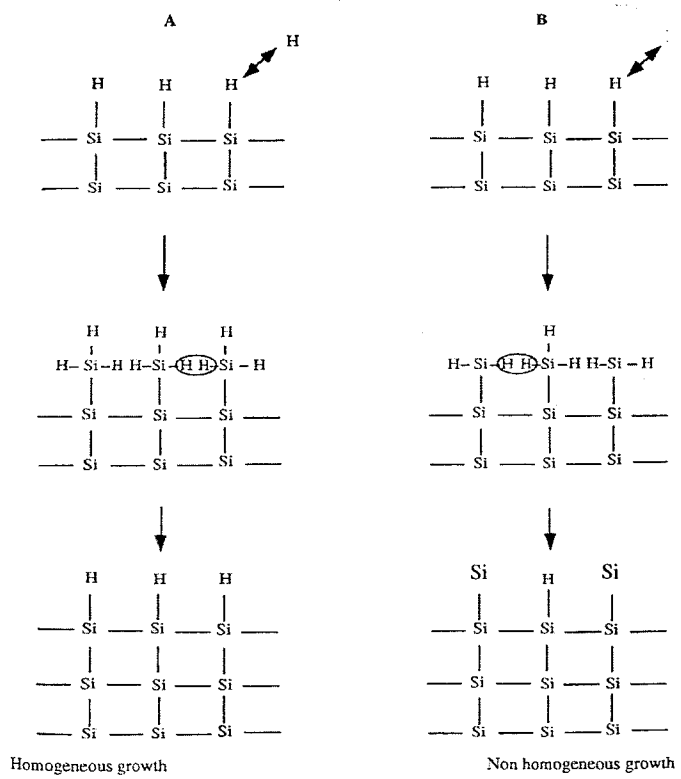

Fig. 2.5 SiH_2 effect on the growth of a-Si:H films [48]

A chemical annealing process helps to remove the excess H on the surface of the Si film during the deposition through ion impinging. According to chemical annealing technique, it consists in growing a thin film, typically 15-30 ′, and then subjecting it to bombardment from plasma, and then repeating the cycle. During the ion treatment period, the highly energetic ions are supposed to break the weak Si-H bonds and take the excess H away by combining them with the H ions. And this in turn reduces the micro-voids induced by the excess H and improves the stability of a-Si:H in the future application.

CHAPTER 3 CHARACTERIZATION

3.1 Film characterization

3.1.1 UV/VIS/NIR Spectroscopy

An ultraviolet/visible/near-infrared (UV/Vis/NIR) spectrophotometer is used to determine the film thickness and the optical band gap from the absorption coefficient variations with photon energy. The system used to obtain the UV/Vis/NIR spectra is a split beam apparatus manufactured by Perkin-Elmer and interfaced to a standard PC. Split-beam spectrophotometers generate a single monochromatic light beam that is then split by optics into two parallel beams of the same incident power. One of the two beams is aimed directly at photo-detector while the other passes through the sample and substrate. The difference in transmission is then measured at the photo-detector as the difference in the two beam powers.

The light not transmitted through the sample and collected is either reflected or absorbed. The substrate also reflects light, and as a result an interference pattern is observed in the transmission vs. wavelength spectra as shown in figure 3.1. The interference can be used to determine the thickness of the film by comparing the positions of adjacent peaks or valleys as in equation 3.1 [49]. In equation 3.1,

$$t = \frac{(\lambda_1 \lambda_2).m}{(\lambda_1 - \lambda_2).n} \qquad (3.1)$$

m=1/2 for peak to peak and 1/4 for peak to valley (Fig. 3.1) and n is the refractive index of the material. The refractive index varies with wavelength and can be calculated from the average value of reflection. Growth rate for the sample thus can be obtained diving the thickness by deposition time, assuming uniform deposition time.

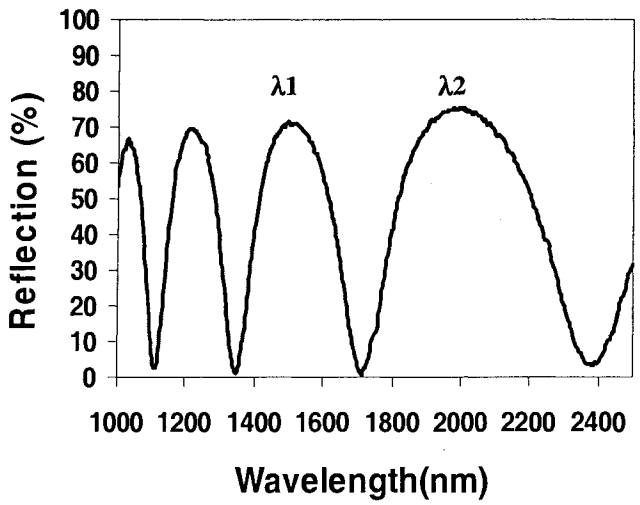

Figure 3.1 Thickness extracted by transmission spectroscopy

In addition to the film thickness, the absorption coefficient can be obtained through UV/Vis/NIR. The absorption coefficient as a function of wavelength can be calculated using the following expressions for the absorption and transmission as a function of the wavelength of the incident photons.

$$T(\lambda) \approx (1-R)e^{-\alpha(\lambda)t} \qquad (3.2)$$

$$A(\lambda) = \log_{10}\frac{I_i}{I_t} = \log_{10}\frac{1}{T(\lambda)} \qquad (3.3)$$

where $A(\lambda)$ is called optical density, $T(\lambda)$ is the transmission and t is the thickness of the film, and $\alpha(\lambda)$ is the absorption coefficient. From (3.2) and (3.3), the absorption coefficient can be given as

$$\alpha(\lambda) = \frac{\ln(1-R(\lambda)) + 2.303A(\lambda)}{t} \qquad (3.4)$$

Once the absorption coefficient is known for a range of wavelengths, the material's band gap can be estimated. The optical gap can be approximated as the energy where the

absorption coefficient is equal to10^4 cm^{-1}, known as the E04 energy. This is a simple method of estimating the band gap of the material as its determination is made graphically from a plot of the absorption coefficient α vs. photon energy, such as figure 3.2. Care must be taken however to account for the reflection interference seen at lower energy values, as the actual absorption spectra is the difference of the curve traced by the top of the peaks and the curve formed by the bottoms of troughs caused by interference.

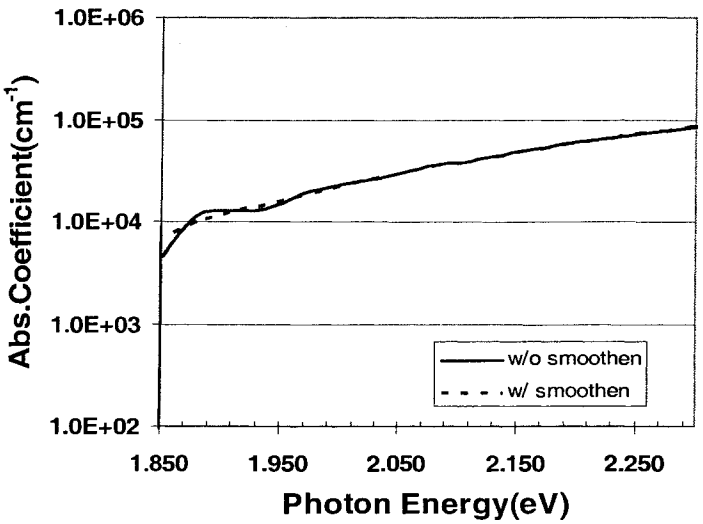

Figure 3.2 E04 energy derived from absorption coefficient

The band gap of the material can also estimated using Tauc's expression, shown in equation 3.5, which describes the absorption that occurs at photon energies above the E04 energy. The E_{tauc} energy can be determined by plotting $(\alpha\hbar\omega)^{1/2}$ as a function of the energy of the energy of incident photons, then finding the intercept of that line with the x-axis.

$$\alpha\hbar\omega = B(\hbar\omega - E_{Tauc})^2 \qquad (3.5)$$

These two approximations for the material's band gap should agree, in general, E_{tauc} is ~0.15 eV less than E04 for hydrogenated amorphous silicon. A typical plot used for the

determination of Tauc's gap is shown in figure 3.3. Tauc's gap is a more ambiguous measure of band-gap experimentally as the slope of the linear region is sometimes difficult to determine. It is important to measure the band gap as deposition parameters change because it gives an indication to the degree of crystallinity of the material, and the amount of hydrogen incorporated into the film. The E04 energy is preferable for reporting bandgap data as it has much less experimental ambiguity, though Tauc gap is closer to the mobility gap, namely the gap between extended conduction band and extended valence band.

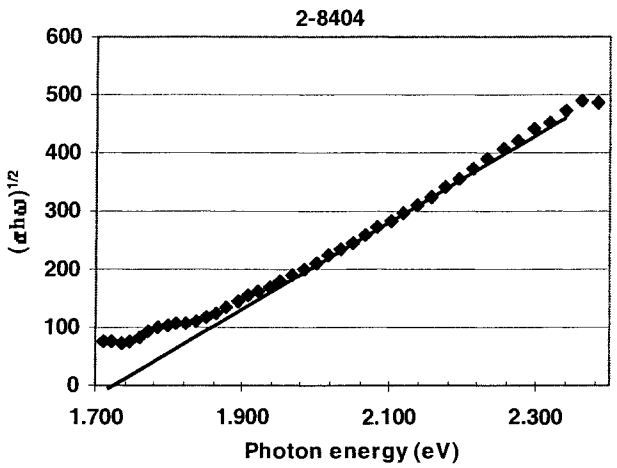

Figure 3.3 Tauc energy derived from UV/VIS/NIR spectrum

3.1.2 Raman Spectroscopy

Raman spectroscopy is a very useful nondestructive technique for determining the degree of crystalline quality of the films. In this technique a laser beam is used to illuminate the specimen. Scattered light is collected by the detector in front of the sample. Most of the light scattered is of the same frequency as the incident light. This is called Rayleigh scattering and is not useful in this measurement. Another type of scattering involves

phonons, which are lattice vibration quanta. In this type of scattering a phonon is either created or annihilated by the incident photon. It is this type of scattering that produces the useful Raman spectra. The energy and momentum conservation equations for such a process are shown in Equation 3.6 and 3.7, where the subscripts s, i, and p refer to scattered, incident, and phonon, respectively.

$$\hbar\omega_s = \hbar\omega_i \pm \hbar\omega_p \qquad (3.6)$$

$$\hbar k_s = \hbar k_i \pm \hbar q_p \qquad (3.7)$$

In the above equations the minus sign refers to a process that creates a phonon and is called Stokes scattering; the plus sign refers to a process that destroys a phonon and is called anti-Stokes scattering.

Photon momentum is very small compared to the width of the phonon Brillouin zone. Momentum conservation limits the Raman scattering to a very narrow band of allowed frequencies at the center of the Brillouin zone. For crystalline silicon there is only one active phonon mode at $520cm^{-1}$ and hence only one peak at this value in the Raman spectrum [50]. Amorphous silicon can have a variety of phonon modes, with the most intense peak located at $500cm^{-1}$. Therefore from the position and shape of the Raman peak we can determine whether the material is crystalline, amorphous, or of mixed phases. Figure 3.4 shows the spectra of a microcrystalline silicon film and an amorphous silicon film.

In addition to the peak position, peak width defined by full width at half maximum (FWHM) is a very useful parameter for the Raman spectrum. It gives an indication of the crystalline quality of the material. As the material becomes disordered, relaxation of the momentum conservation limitation on the phonon mode occurs. As a result, the Raman peak

begins to broaden. By looking at the change in peak width of a film with respect to the germanium wafer, the crystalline quality of the film can be evaluated.

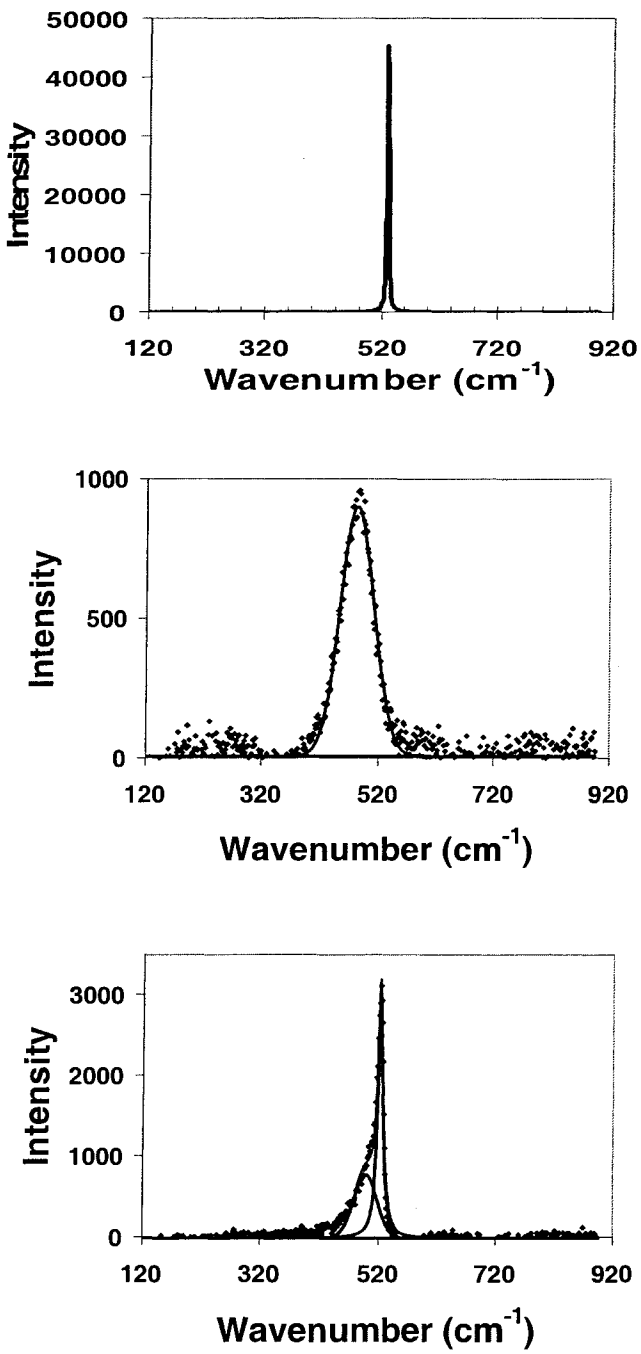

Figure 3.4 Raman spectrums of c-Si (top), a-Si (middle) and nc-Si (bottom)

3.1.3 X-Ray Diffractometry

Crystalline material is composed of atoms arranged in a periodic lattice structure. The atoms can be viewed as being on a series of evenly spaced parallel planes. When X-ray is incident on the material, diffraction pattern can be produced by the planes since the spacing of these planes is close to the wavelength of the X-ray. Peaks appear at angles satisfying Bragg's law

$$n\lambda = 2d\sin\theta \qquad (3.8)$$

where λ is the wavelength of the X-ray, d is the spacing of the planes and λ is the angle between the incident beam and the surface of the sample. The peaks are the result of constructive addition of the waves reflected by the planes. Since λ can be precisely determined and λ is known, d can be accurately obtained. For cubic system, the lattice constant a is then calculated from the equation

$$d = \frac{a}{\sqrt{h^2 + k^2 + l^2}} \qquad (3.9)$$

where h, k and l are Miller indices of the plane.

The typical X-ray diffraction patterns of a-Si, c-Si, and nc-Si are shown in Figure 3.5. From the above discussion we can see X-rays can also be used as a way to determine whether or not there is crystalline phase in the material by observing whether or not peaks appear at specific angles because only crystalline materials have periodic lattice and therefore clearly defined planes. Furthermore, grain size of the material can be estimated from the width of the peaks using Scherer's formula [51],

$$t = \frac{0.9\lambda}{B\cos\theta_B} \qquad (3.10)$$

where λ is the x-ray wavelength, B is the full width at half maximum and θ_B is the diffraction angle. Although the grain size thus obtained is only a rough estimation, comparisons between different samples can be made. Further information about the samples can be obtained regarding texture, strain and preferred orientation by the relative intensities of different peaks. A schematic diagram of the calculation of grain size based on Scherer's formula is provided in Fig. 3.6.

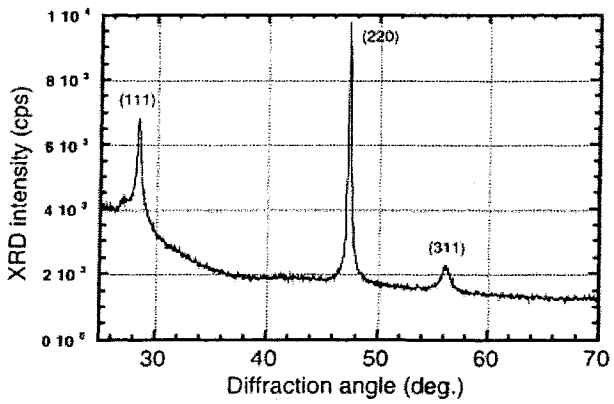

(a)

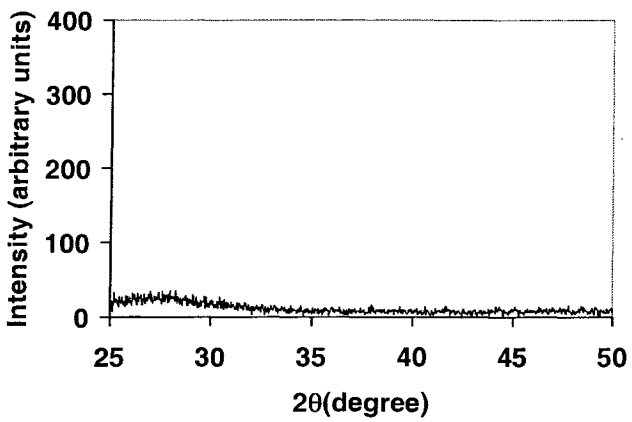

(b)

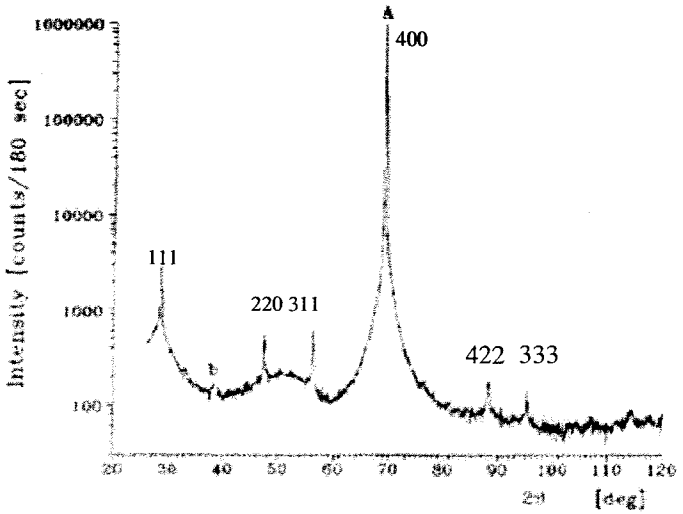

(c)

Figure 3.5 X-ray diffraction spectra for nc-Si(a) [52], a-Si(b), and c-Si (c) [53]

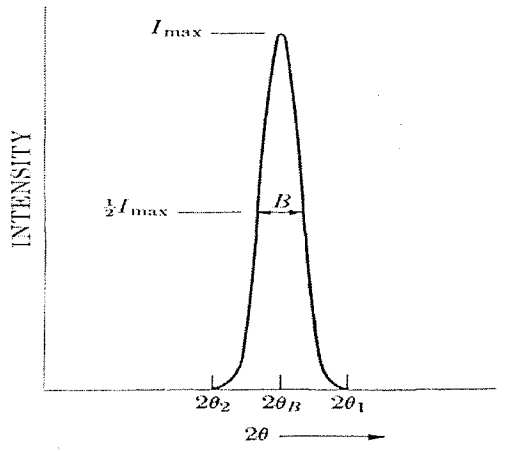

Figure 3.6 Schematic diagram of Scherer's formula [51]

3.1.4 Activation Energy

The conductivity of a semiconductor is proportional to the number of carriers available to transport charge from one reservoir to another, such as from one ohmic contact

to another located some distance away. Since the intrinsic concentration of carriers is dependent upon temperature, conductivity should vary with the material temperature according to an Arrhenius relationship. Using the definition of conductivity equation, it is easy to relate the conductivity of a semiconductor under steady bias to temperature though equation 3.11, where E_A is activation energy, k is Boltzman's constant, T is the temperature in Kelvin, and σ_0 the baseline conductivity, or pre-exponential factor.

$$\sigma = \sigma_0 e^{\frac{-E_A}{kT}} \quad (3.11)$$

For amorphous, lightly doped semiconductors, the vast majority of electrons will be located in states at or below the Fermi energy and since it is these carriers that need to be energized into the conduction band for current to flow, E_A is a measure of the location of the Fermi energy in these materials.

When measuring this parameter, the sample is placed on a heated aluminum block and a spring-loaded contact is placed on each side of the coplanar contacts described earlier. The sample is then sealed in a light impervious box and heated to ~ 210°C and then a 100V bias applies. Current measurements are taken from 210°C to 130°C in 10 degree increments and then Ln(I) is plotted vs. 1/T. This plot is then modeled by linear regression and the slope of that line multiplied by K to determine the activation energy. High quality a-Si:H materials typically exhibit activation energies approximately 0.9 eV, while a-(Si,Ge):H materials exhibit activation energies of approximately one-half their E_{04} bandgap.

3.1.5 Photo and Dark Conductivity Measurements

Determining the suitability of hydrogenated group IV alloy thin films for electronic applications begins by examining the conductivity of the material under illumination and comparing it to the material's conductivity under dark conditions.

This ratio of conductivity is known as the photosensitivity of the material and is a general indication to the quality of the material as high quality a-Si:H has a photosensitivity greater than 10^5, a-(Si,Ge):H with an E04 gap of 1.5 ev is ~10^2, and doped crystalline silicon or germanium should be ~1. A large increase in the absolute conductivity of the material should be seen as crystalline nature of the material varies from amorphous to single crystal material as the carrier concentration, mobility and lifetimes of the crystalline material are much greater than the amorphous material.

The light and dark conductivity measurements are performed in an apparatus consisting of a large aluminum heat sink cooled by a fan placed in a light impervious box. Two spring-loaded probes are then placed on the co-planar metallic contacts described in the contact deposition section. These probes are connected to a Keithly 617 electrometer and a Keithly 230 voltage source to supply a 100V bias between the two coplanar contacts and measure the small resulting current. Steel panels and an aluminum door sealed with Velcro and magnets enclose the sample and heat sink to form the light-tight box that prevents light from striking the during the dark conductivity measurement. The photo current is measured by turning on a quartz lamp directly above the sample that has a calibrated aperture between itself and sample so that 100 mW/cm2 is incident upon the sample, which is the standard AM 1.5 illumination that is reported in literature for photoconductivity.

The conductivity is calculated as shown in equation 3.12 by multiplying the width between the coplanar contacts (W) with the current measured (I) during the test.

$$\sigma_{L,D} = \frac{WI}{LVt} \qquad (3.12)$$

This product is then divided by the product of the contact length, applied voltage, and the film thickness. For these experiments, the ratio of L/W was 20.

3.1.6 Fourier transform infrared spectroscopy

Fourier-transform infrared spectroscopy is a very informative tool to detect the composition, the microstructure, and the content of materials. It is used here to determine the H content and the silicon-hydrogen bonding configurations.

When photons in the mid infrared range with wavelengths ranging from5 to 50 μm are incident on a hydrogenated silicon film, the photons may be directly absorbed at the band features, by phonons, free charge carriers, or impurities. In the mid-infrared region, the interaction with the sample results in rotational and vibration transitions of the molecules. The wavelength of the absorption peak corresponds to specific chemical bond and mass of atoms. The spectral distribution of the absorption peaks of various silicon-hydrogen boning modes has been identified by Brodsky et al [54] and can be roughly categorized into three modes: (1) the Si-H and Si-H_2 stretching mode (2000-2100cm^{-1}), (2) the SiH_2 and SiH_3 bond bending scissors mode (840-890cm^{-1}), and (3) the Si-H wagging mode (640 cm^{-1}).

The most common method to calculate hydrogen content has been proposed by Brodsky, Cardona and Cuomo (BCC) [55]. Double-side polished Si wafers were used for

original IR study, which prevents diffuse reflection from the backside of the substrate. The following equation gives the hydrogen content in a-Si:H [56]:

$$N_H = A\int \frac{\alpha(\omega)}{\omega} d\omega \qquad (3.13)$$

where A is an experimentally determined constant and for wagging mode is 1.6×10^{19} (cm^{-1}), $\alpha(\omega)$ is the absorption coefficient at angular frequency ω. The integral extends over the whole $640cm^{-1}$ absorption peak.

3.1.7 Urbach energy

Urbach energy of valence band tails and mid-gap defect densities are important parameters for determining the performance of a-Si:H devices. In particular, the tail states limit the movement of level upon light excitation, and thereby provide a limit to open-circuit voltage that can be developed in an a-Si:H solar cell. The mid-gap states provides a very effective recombination-mechanism for excess carriers, and thus tend to limit the diffusion length of minority carriers, and hence fill factor and open circuit voltage in solar cells. A high density of mid-gap states also reduces the electric field in the middle of the device, thereby reducing the range ($\mu\tau\varepsilon$) of the minority carriers.

Since Urbach energy is a good measure of the material quality and a good quality material should have lower Urbach energy, many methods have been explored to measure it. The traditional way to measure Urbach energy of films is based on sub-gap photoconductivity techniques, which rely on optical excitation from these states, into conduction band and then measuring photoconductivity of the material versus wavelength of light.

This measurement relies on the dual-beam photoconductivity technique developed by Wronski et al. [57], where a strong DC beam is used to fix the quasi-Fermi levels of the material, keeping available states in the mid-gap region filled with photo-generated carriers. The second beam is an AC beam fixed at 13.5 Hz by a chopper to remove noise associated with the 60 Hz current used to power the equipment. The beam from the light source is then modified by diffraction grating in a monochrometer to produce a narrow wavelength spectrum that is then aimed at the film between the coplanar contacts to supply additional carriers and increase the material's conductivity. The AC beam, after passing through the monochrometer and chopper, passes through a series of high pass filters to reduce the harmonic frequencies associated with the beam exiting the monochrometer, and to prevent low-wavelength light from reaching the sample until it is desired. The wavelengths used for typical a-Si:H characterization varies from 1200 nm to 600 nm, and filters with roll-off frequencies of 700 nm, 900 nm, and 1200 nm are used. A schematic of the device used in the dual-beam photoconductivity technique is shown as Fig. 3.7.

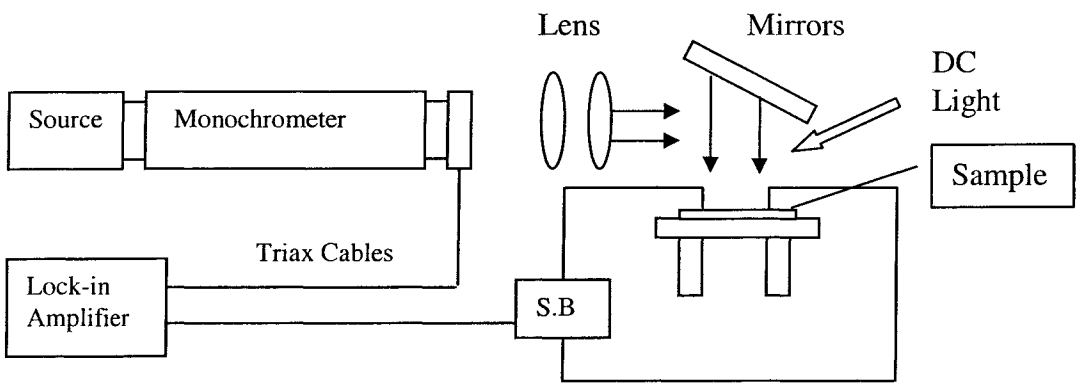

Figure 3.7 Apparatus for measuring QE using two-beam photocurrent technique

The AC light beam is collimated through lenses and focused onto the sample by a mirror. The care taken to ensure the quality of this AC beam is critical, as the additional current generated by it is measured with a lock-in amplifier to determine the absorption coefficient as a function of photon wavelength. From this absorption coefficient data, the Urbach energy (E_{ur}) can be determined from equation 3.14, where E_g is the band-gap, h is Planck's constant and ν the wavelength.

$$\alpha = \alpha_0 \exp\frac{h\nu - E_g}{E_{ur}} \qquad (3.14)$$

The inverse slop of the natural logarithm of absorption coefficient α versus photon energy gives us the Urbach energy. For a good sample, the Urbach energy is in the range of 45meV, while for a bad sample the Urbach energy is usually larger than 50meV[42].

3.2 Device Characterization

3.2.1 I-V Curve

The performance of a solar cell under illumination can be described by current voltage dependence. A typical current-voltage current of a p-i-n solar cell under illumination is shown in Fig 3.8. From the equivalent circuit was shown in Fig 1.3, we can use three parameters that give a rather complete description of the electrical behavior.

From the equivalent circuit, the current-voltage characteristics of the device is given by

$$J(V) = J_s[e^{\frac{qV}{AkT}} - 1] - J_L(V) \qquad (3.15)$$

where J(V) is the current J at voltage V, J_s is the reverse saturation current, q is the electronic charge, A is the diode factor, K is Boltzman's constant, T is the temperature and J_L is the light generated current.

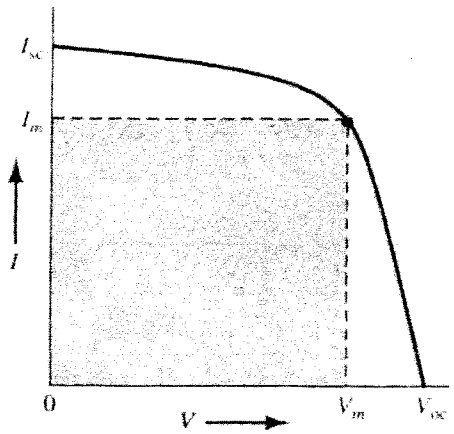

Figure 3.8 I-V Curve of an illuminated p-i-n diode [3]

The first parameter is the short circuit current J_{sc}, which is the current of the cell under illumination for V=0, i.e., in the equivalent circuit, the load is taken away and the loop to hold the load is thus open. In this circumstance, the $J_{sc}= J_L(0)$.

J_L, the photo-generated current, or the short-circuit current, depends on the spectrum of the incident light, the materials response to the light and the collection efficiency. It can be written as

$$J_L = q\int (1-R)Q(E)S(E)dE \qquad (3.16)$$

where R is the reflection coefficient, S(E) is the spectrum of the light source and Q(E) is the collection efficiency of the cell.

A high short circuit current requires good material quality and an optimal design of the cell to absorb and trap as many incident photons as possible.

The second parameter is the open-circuit voltage V_{oc}, which is obtained for J(V)=0, i.e., in the equivalent circuit, the loop with the load now is short.

From (3.15), Voc can be expressed as

$$V_{oc} = \frac{AKT}{q} \ln(\frac{J_L}{J_s} + 1) \qquad (3.17)$$

For a diode junction dominated by depletion, the saturation current can be defined as [58]

$$J_s \approx \frac{q n_i W_d}{2\tau} \qquad (3.18)$$

where $$n_i = \sqrt{N_C N_V} \exp(\frac{-E_g}{2KT}), \qquad (3.19)$$

So, Voc can be defined as:

$$V_{oc} \approx \frac{KT}{q} \ln(\frac{J_L}{J_s}) \approx \frac{KT}{q} [\ln(J_L) - \ln(\frac{qW_d}{2\tau} \sqrt{N_C N_V})] + \frac{E_g}{2q} \qquad (3.20)$$

where n_i is the intrinsic carrier density, E_g is the band gap, W_d is the depletion width of the junction. From (3.20), it can be shown that E_g is a dominant factor to decide V_{oc}, while lifetime and thickness affect the open-circuit as well. Typically, a well-designed a-Si:H solar cell can provide a open-circuit voltage in the order of 0.9V. A high open-circuit voltage requires efficient doping in the p+ and n+ layers (which gives higher built-in voltage), a high bandgap and also good interface.

The third parameter is fill factor (FF). The maximum possible current and the maximum possible voltage in the solar cell are I_{sc} and V_{oc}, respectively. Fill factor provides the ratio between the real optimum output power P_{max} ($=I_m \times V_m$) and the ideal optimum output power P ($=I_{sc} \times V_{oc}$), and it is defined as

$$FF = \frac{V_m I_m}{I_{sc} V_{oc}} \qquad (3.21)$$

Therefore, the larger the FF is, the more "square-like" the current-voltage is. The fill factor provides an indication of the quality of the materials used in the i-layer, and how well the solar cell is designed. A high fill factor needs low loss of photogenerated carriers in the I-layer and at the interfaces, strong electric field in the i-layer, and a good ohmic contact. High quality a-Si:H solar cells with proper p-i interface designs have fill factor values of about 65% to 70%.

Based on Voc, Isc, and FF, the energy-conversion efficiency η of the solar cell can be calculated. It is defined by the ratio of maximum power that is extracted from the cell to the total illumination power. The equation is

$$\eta = \frac{FF.V_{oc}.I_{sc}}{P_{in}} \qquad (3.22)$$

where P_{in} is the total incident power of the photons. In this project, the area of the cells is around 0.08 cm2, the light source used for I-V measurement is an ELH lamp operating at 115V, 2.4A.

3.2.2 Quantum efficiency

The quantum efficiency (QE) measurement is another useful diagnostic tool to characterize the performance of solar cells. Quantum efficiency is defined as the ratio of the number of charge collected to the number of photons incident on the sample at a particular wavelength.

Considering a p-i-n diode, if the incident photons are from the p+ layer, the equation to descript the QE is

$$QE\ (\lambda, V) = \int_0^t \alpha(\lambda).e^{-\alpha x}.e^{-\int_0^x \frac{1}{\mu\tau\varepsilon(y)}dy}.dx \quad (3.23)$$

where α is the absorption coefficient and it is a function of photon wavelength λ, μ is the carriers' mobility, and τ is the carriers' lifetime, t is the thickness for i layer, and ε (y) is the electric field at point y.

To measure QE, the setup used is shown in Fig 3.8. The sample under test can be biased at forward or reverse voltages or be grounded. Normally, the device currents are measured over the visible wavelength range of 400nm<λ<800nm, at steps of 20nm, since this range covers the major portion of the solar spectrum to which the material responds. The forward and reverse bias voltages can be applied to the cell to simulate operation conditions and to enhance the internal electric field, respectively.

QE measured at zero bias voltage provides important information about the cell. The thickness of the p+ layer by looking at the QE values at short wavelengths (400nm) can be intuitively checked. Too thick a p+ layer would lead to a very low QE value and too thin a p+ layer would result in unreasonably high QE. The generally accepted QE value at short wavelength is about 0.5-0.6 for a 10nm thick p+ layer. QE values at long wavelengths (~700nm) tell us about the collection efficiency for long wavelength photons. This is affected by the reflection due to the texture of the substrate. It is also affected by the material quality of i-layer. Finally the position of the maximum QE in the spectrum is usually associated with the thickness of i-layer. When the thickness of i-layer is reduced, the maximum QE position will shifts towards shorter wavelengths. For a cell with about 350nm of i-layer, the maximum

QE point is located at ~540-600 nm. Figure 3.9 gives a typical QE spectrum of a-Si:H solar cells.

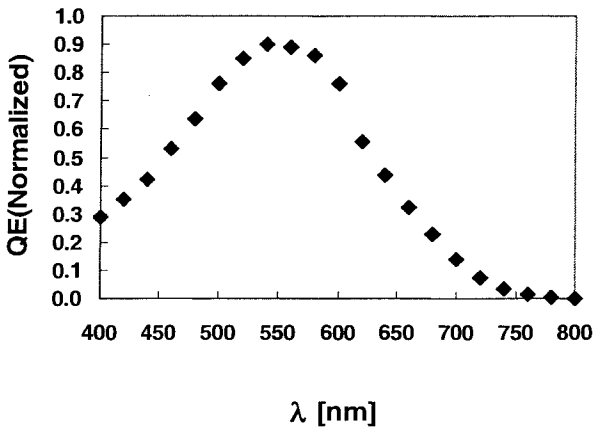

Figure 3.9 QE spectrum of an a-Si:H solar cell

QE measured under bias can tell us about the electric filed profile inside the cell. When the solar cell is under forward bias, the internal electric field is reduced. As a result, the carrier collection efficiency (especially of those created away from the p-i interface) is reduced since the carrier collection of a-Si:H solar cell relies on the assistance of the electric field because of low $\mu\tau$ products, and therefore diffusion lengths for higher wavelengths. The electric field enhances the effective carrier diffusion length (for nanocrystalline device) or range (i.e. $\mu\tau\varepsilon$, for amorphous device). For a high quality solar cell, the internal electric field is so strong that a small forward bias applied to the cell will not affect the carrier collection efficiency to a great extent.

The ratio of the QE (λ) values under zero to positive bias can provide information about how well the device absorbs and collects the photons of various wavelengths at various locations in the cell. Since the photons are incident on the p-layer, the lower energy photons

are absorbed further from the p-layer than the higher energy photons. As a result, these photogenerated holes must drift further across the i-layer before they are collected in the p layer. If the QE ratio at these wavelengths is high, it is an indication that the holes were being generated but were not being collected without the extra field-assist provided by the negative bias. Low QE ratio indicates that the material is of high enough quality to collect the holes even at positive bias. Also if the ratio is high at shorter wavelengths, the problem can be pinned on the p-layer or p-i interface. Figure 3.10 gives two QE ratio curves. One is from a good quality a-Si:H solar cell and the other is from a poor cell.

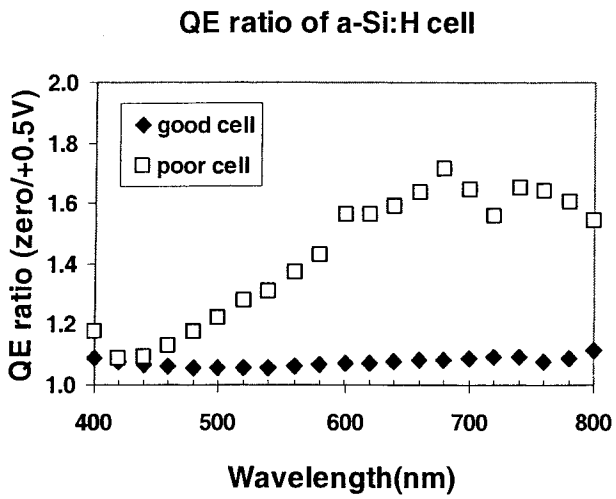

Figure 3.10 QE ratio of a-Si:H solar cells

From this figure, it can be seen that the QE ratio of good cell is almost equal to one through all the wavelengths, which means that external positive bias has very small impact on the carriers' collection, and the cell has strong enough internal electrical field to collect the generated carriers even under a positive bias. However, for the poor cell, the QE ratio keeps increasing with the wavelength, and this tells that the cell encounters problem with carrier collection, especially in long wavelength region. The increased QE ratio indicates a

poor internal electrical field, thus poor quality of the cell. The poor internal electrical field can easily be affected by the external positive bias, and this in turn damages the transportation of the generated carriers in the intrinsic layer of the cell, and correspondingly, QE ratio increases.

3.2.3 Hole μτ product

The μτ product of holes is a very important parameter for devices. At the most of condition, the holes are minority carriers in solar cells except the region of p-i interface. It is the quantity that primarily determines the fill factor and the behavior of the QE ratio of the cell. Large μτ product means that the holes can drift longer with the assistant of the internal field and be collected by the p+ layer before they are trapped and recombined. From equation 3.23, it can be seen that QE is closely related to the hole range, μτε. QE value can be obtained by measurement mentioned above, and the thickness of the i layer, absorption coefficient can be measured as well. If the electric field is known, the μτ product then can be derived from equation 3.23.

There are various methods of obtaining the electric field profile. Hack and Shur profiled the electric field successfully using a computer model [59]. This model includes a boundary condition at the interface, and requires a numerical integration of the defect density profile over a range of energy, and then the electric field profile is written as a function of distance, through the voltage and distance relationship. It shows that the electric field is high near the interface and drops down quickly in the middle. Since the electric field near the interface of p-i contributes little to the carriers' collection, and only the electric field in the bulk of the I-layer plays major role, Greg Baldwin used a simper version of this model,

where no boundary condition is used, and electric field can be obtained directly from an expression of voltage [60]. Figure 3.11 gives a simulated electrical field profiles in p-i-n diode based on H&S model [59].

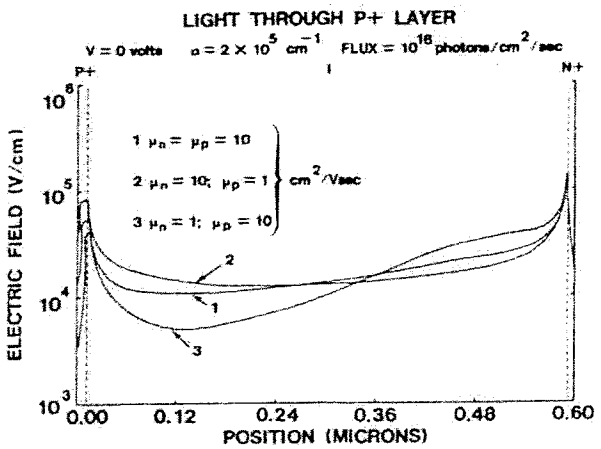

Figure 3.11 Simulated electric field profiles in p-i-n diode for varying values of the carrier band nobilities [59].

Although these models profiled the field more accurately, they are not simple to use for device design and $\mu\tau$ product calculation, and since the field values cannot be obtained directly as a function of distance and there is no closed form expression for the electric field, the calculation can become very complicated. In general, a uniform field approximation is used. Dalal and Alvarez used a uniform electric field approximation by divided the sum of the applied and diffusion voltage by the thickness of i-layer [61]. Crandall also used a similar approximation to obtain the filed profile [62]. In calculation this average uniform field, the influence of strong fields at interface (and therefore volt drops) as shown by H & S model is included.

If a constant electric field were applied, the equation 3.23 would be [61]:

$$QE(\lambda) = \frac{\alpha S_n}{1+\alpha S_n}[1-\exp(-\frac{t}{S_n}(1+\alpha S_n))] \qquad (3.24)$$

where $S_n=\mu\tau\varepsilon$ is the range of holes.

The basic principle of the measurement is therefore simple [61]. We measure the quantum efficiency of the device for several wavelengths, as a function of applied voltage. Under reverse bias, the QE increases, and under forward bias, it decreases. If we assume that $\mu\tau$ doesn't change with bias voltage and wavelength, the QE variation solely comes from the change of the electric filed profile. Under one specific wavelength, under different bias, we get a set of points from the measurement. Concurrently, by employing the biases (i.e. electric field) into equation 3.24, we can get another set of data if the $\mu\tau$ is known. With the trial and error method, a suitable $\mu\tau$ can be picked up to let the measurement curve match the simulation curve, and this $\mu\tau$ product is the desired one. In the measurement, long wavelengths such as 600nm-800nm should be applied. For the short wavelength, most of the photons are absorbed near the p-i interface, where the recombination becomes important and the model is not hold. The model requires that all wavelengths must yield the some $\mu\tau$ product. Figure 3.12 gives $\mu\tau$ product measurement result of one a-Si:H cell based on the procedures mentioned above.

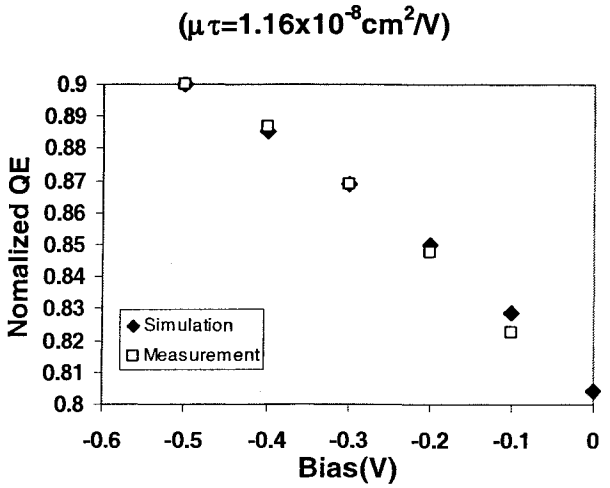

Figure 3.12 μτ measurement of a-Si:H solar cell

3.2.4 Urbach energy

The characterization of devices' urbach energy follows the similar procedure described in chapter 3.2.2 which is designed for the quantum efficiency. The only different between the QE measurement and urbach energy measurement is that urbach energy is measured in a long photon wavelength range, normally from 600nm to 1200nm for a-Si. A long wavelength range is applied in order to pick up the tail state information. From equation 3.23, it can be seen that QE is a function of absorption coefficient. Therefore the QE versus photon energy measurement gives the relation between absorption coefficient and photon energy, and follows the equation 3.14 as well. The urbach energy from devices is obtained by the inverse slop of the natural logarithm of QE data versus photon energy.

Figure 3.13 gives the Urbach energy measurement result of one a-Si:H solar cell based on the method mentioned above and the obtained value is 47meV.

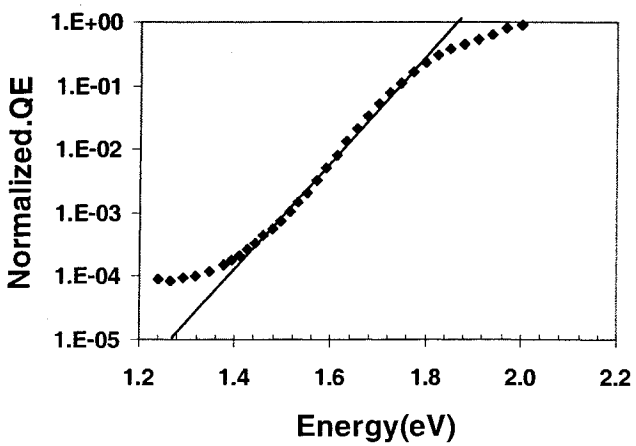

Figure 3.13 Urbach energy measurement of a-Si:H cell

CHAPTER 4 FILMS RESULTS

4.1 He Plasma Sample

4.1.1 Microstructure properties

It has been shown that the amorphous films become more ordered when they are subjected to H plasma [63]. However, in the work with He plasma, it is found that when we increased the cycle time for annealing, the microstructure of the materials changed significantly; the films became nanocrystalline as measured using Raman spectroscopy and x-ray diffraction.

The deposition parameter in each cycle is shown as follows:

		He	SiH_4	ppm TMB	H_2(i)
Growth period time	(t1)	25%	15%	15%	10%
Annealing period time	(t2)	25%	0%	15%	0%

Figure 4.1 shows the schematic view of chemical annealing process.

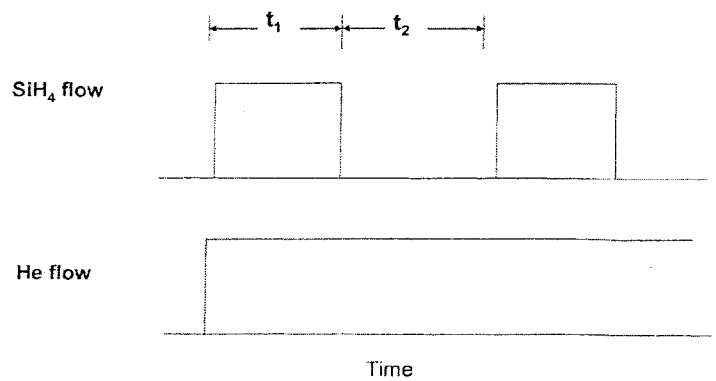

Figure 4.1 schematic view of chemical annealing process

The reason that H_2 from intrinsic line is introduced is that previous work shows the necessity for having both H and He present to prepare good films [30]. The measurements of one sequence films are provided in Table 4.1

Table 4.1 X-ray and Raman measurement for He CA films

Sample No	Temperature (°C)	Pressure (mT)	t1/t2	Thickness (um)	Grain size (111)	Grain size (220)	$520cm^{-1}/490cm^{-1}$ peak ratio
8287	315	15	10s/10s	0.85	N/A	N/A	N/A
8285	315	15	10s/20s	1.0	88	54	3.09
8286	315	15	10s/30s	1.1	82	59	3.33
8304	315	15	10s/40s	1.1	91	67	3.6
8305	315	15	10s/50s	1.0	95	65	3.63

X-ray diffraction

From table 4.1, it shows that a dominate grain size in <111> direction than <220>. The corresponding X-ray data shown in Fig.4.2 gives a sharper <111>peak than <220> peak. We know that higher the ratio of $520cm^{-1}$ peak over $490cm^{-1}$ peak in Raman spectrum for nanocrystalline silicon films, the more crystalline tissue is introduced. From the values shown in table 4.1, it can be seen that the crystalline tissue increases as the annealing time increases. Moreover, it shows that a 10 second annealing time in each cycle is not enough to give crystalline tissue.

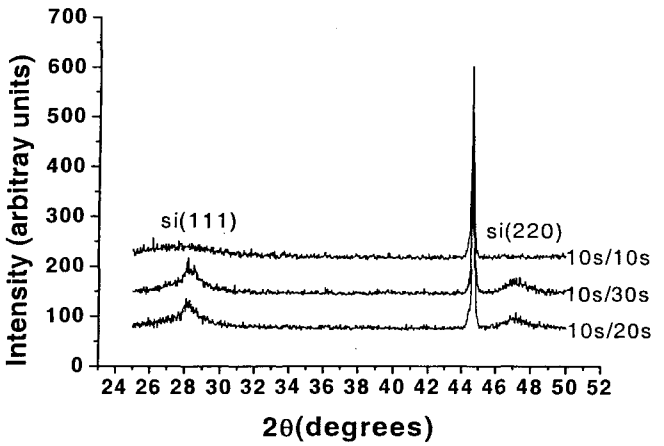

Figure 4.2 X-ray spectra for 8285-8287, sharp peak at 45°C is due to steel substrate.

Raman Spectra

Raman spectra for these samples are shown in Figure 4.3. 2-8287 was subjected to 10s anneal and shows amorphous structure. 2-8285 was subjected to 20s annealing and shows a significant crystalline fraction. Figure 4.4 shows the Raman peak ratio as a function of annealing time. The peak ratio is of c-Si peak at 520 cm^{-1} to a-Si shoulder at 490 cm^{-1}.

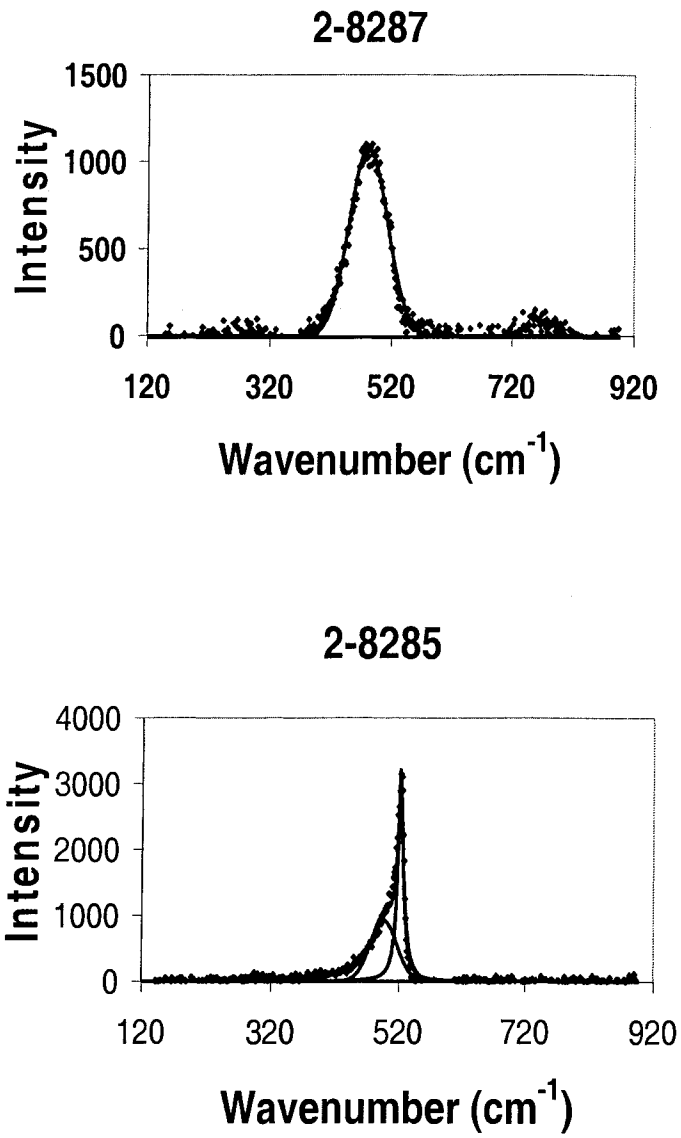

Figure 4.3, Raman spectrums for He CA films, top is amorphous and bottom is nanocrystalline structure.

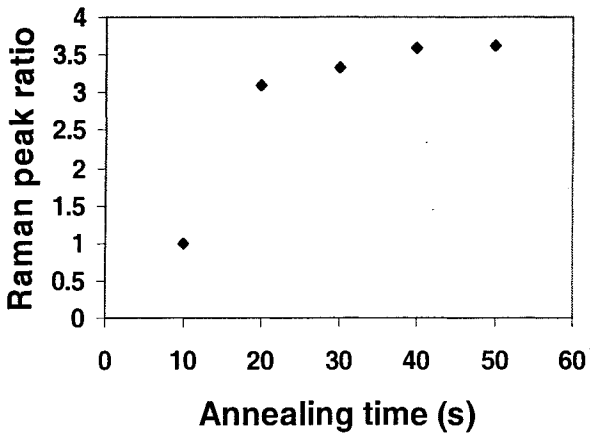

Figure 4.4, Raman peak ratio as a function of annealing time.

H bonding

We studied the hydrogen bonding in these materials by growing layers on polished Si wafers. In Fig. 4.5, we show the FTIR absorption data on three films, a layer-by-layer film subjected to a short (10s) anneal cycle, a film subjected to a 20s annealing cycle, and a film subjected to 30 s annealing cycle. It is very clear from the data that the film subjected to a short cycle shows the classical FTIR signature of a prominent Si-H absorption peak at 2000 cm^{-1}, whereas the film subjected to a longer cycle (20s and 30s) also shows that the characteristic 2100 cm^{-1} peak generally found in nc-Si:H increases. This peak is attributed to bonding at grain boundaries. Thus the H bonding data agree with the X-ray and Raman data. Another significant difference is the peak area at 640 cm^{-1}. A 10s annealing cycle gives a higher peak area than 20s and 30s annealing cycles. This correspond to a higher hydrogen content in 10s annealing cycle ($C_{H\%}$=12.7%) than 20s ($C_{H\%}$=7.06%) and 30s annealing cycles ($C_{H\%}$=7.03%). We know that the higher the crystallinity fraction in film, the lower the hydrogen content. Therefore this agrees with the X-ray and Raman data again.

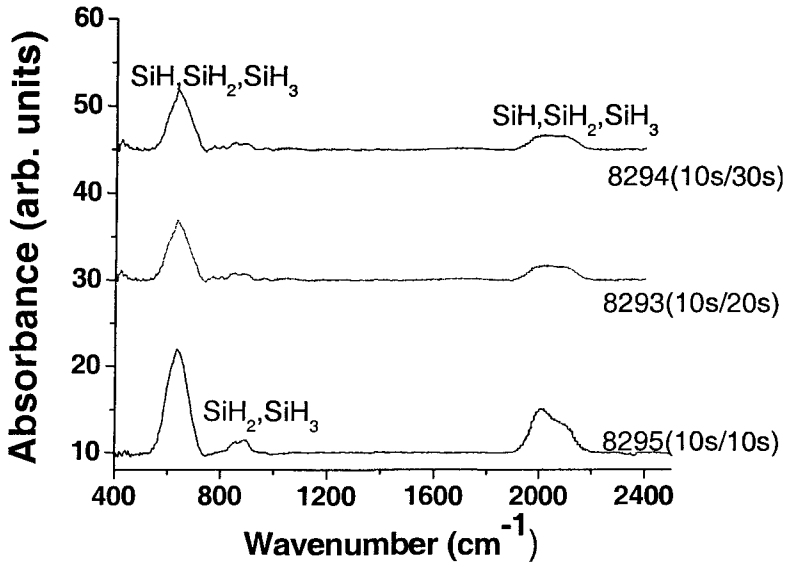

Figure 4.5 FTIR spectra for He CA films.

Since the crystallinity fraction increases with the relative annealing time, we can achieve the same result by decreasing the growth time in each cycle to 8 seconds while keep the annealing time constant. It was found that the ratio of 520cm^{-1} peak over 490 cm^{-1} peaks in Raman spectrum increases, which means a higher crystalline fraction. This result is shown in Table 4.2.

Table 4.2 X-ray and FTIR measurement for He CA films

Sample No	Temperature (°C)	Pressure (mT)	t1/t2	Thickness (um)	Grain size (111)	Grain size (220)	520cm^{-1}/490cm^{-1} peak ratio
8298	315	15	8s/10s	0.95	33	26	1.47
8296	315	15	8s/20s	0.9	75	47	3.35
8297	315	15	8s/30s	1.05	93	60	3.57

Another set of films deposited at the same condition as 4.2 but having a larger thickness was prepared. It is found that the ratio of 520cm^{-1} peak over 490 cm^{-1} peaks in Raman spectrum is not changed significantly. Thus the thickness effect is very small in determining the microstructure structure. The results are shown in Table 4.3

Table 4.3 X-ray and FTIR measurement for He CA films

Sample No	Temperature (°C)	Pressure (mT)	t1/t2	Thickness (um)	Grain size (111)	Grain size (220)	520cm^{-1}/490cm^{-1} peak ratio
8303	315	15	8s/10s	1.5	31	32	1.43
8299	315	15	8s/20s	1.5	65	59	3.42
8301	315	15	8s/30s	1.6	68	49	3.62

The pressure effect is also checked. An increased pressure is supposed to introduce smaller ion energy and this is equivalent to decreasing the annealing time. Therefore a smaller crystallinity fraction is supposed to appear. A pressure of 25mT is applied in the deposition. Compared the peak ratio shown in Table 4.2, a smaller peak ratio was shown for the films deposited at higher pressure. This result is shown in Table 4.4.

Table 4.4 X-ray and FTIR measurement for He CA films

Sample No	Temperature (°C)	Pressure (mT)	t1/t2	Thickness (um)	Grain size (111)	Grain size (220)	520cm^{-1}/490cm^{-1} peak ratio
8323	315	25	8s/10s	1.01	N/A	N/A	1
8324	315	25	8s/20s	1.07	62	43	3.07
8325	315	25	8s/30s	1.06	97	56	3.49

Discussions

It has generally been assumed that one needs the reactive etching effect of H plasma in order to convert an amorphous film into a crystalline film, whether in layer-by-layer growth or by continuous deposition, where one achieves a similar effect by using high dilution ratios in hydrogen/silane mixtures. It is generally found that one needs a high dilution ratio (~20:1) to obtain good crystallinity in continuously grown Si films. As mentioned above, S. Miyazaki et al. [61] reported the amorphous films become more ordered when they are subjected to H plasma. In addition, W. Futako [37] et al. reported the similar result.

In contrast to these results, we induced crystallinity in a-Si:H films by using a non-reactive helium ion beam. We also found that when a hydrogen plasma beam was used instead of a helium beam during deposition and annealing, the resulting films did not become nanocrystalline under comparable annealing cycles. The results of hydrogen plasma samples are provided in chapter 4.2.1.

These results are remarkable, because they contradict the generally accepted assumption that high hydrogen dilutions are needed to crystallize the amorphous films. Instead, what we have shown is that it is the ion flux and energy in a beam that is responsible for crystallization, and that the residual hydrogen in an a-Si:H films is enough to cause any reactivity, such as removal of excess hydrogen from deep within the lattice. The reconstruction of bonds to a more ordered state seems to depend on the presence of ion flux and energy. Note that in the previous work of Miyazaki et al [63], an experiment with a He beam was not done; it is entirely possible that in their case also, it was the ion energy of a hydrogen plasma that was causing better ordering, rather than any reactivity. The present

results support the recent results from our group which showed that at low pressures in a VHF plasma reactor (50 mTorr), one could obtain crystallization of amorphous films at much lower hydrogen dilution ratios (12:1) than normally used (20:1) , but that at higher pressures (200 mTorr and 500 mTorr), one needed the higher hydrogen dilution ratios [64].

These interesting results shown above contradict virtually all the pervious results which ascribe the crystallization phenomenon solely to the presence of excess hydrogen by a reactive etching effect. Rather, it may be a combination of ion bombardment and reactive etching which may be causing the crystallization of amorphous films when high hydrogen dilution is used.

4.1.2 Electrical properties

The deposition parameters of He CA films and non CA films are provided as follows. Since an annealing time larger than 10s gives a nanocrystalline structure, the annealing time is set to 10s.

	Pressure	Temp	He (p)	H_2 (p)	SiH_4 (i)	ppm TMB
He Non CA	25mT	325°C	50%	10%	10%	15%

He CA	P	Temp	He (p)	H_2 (p)	SiH_4 (i)	ppmTMB	H_2(i)
Growth time (10s)	25mT	325°C	50%	10%	10%	30%	10%
Anneal time (10s)	24mT	325°C	50%	10%	5%	30%	10%

It should be noted that H_2 (p) means a 10% hydrogen from plasma line of the PE CVD system, and H_2 (i) means 10% hydrogen from intrinsic line. As mentioned above, it is necessary to have both H and He present to prepare good films. So 10% hydrogen from

plasma line was introduced. 10% hydrogen from intrinsic line was introduced because this will help flush out the SiH_4 gas during annealing period and decrease the switch time between growth period and annealing period. During the growth period, the pressure is 25mT and it is 23mT for annealing period.

Comprehensive measurements are carried out, which includes stability, conductivity, E04, Tauc energy, activation energy, Urbach energy, midgap absorption coefficient. Table 4.5 gives the summary of these properties of He non CA films and He CA films.

Table 4.5, properties of He films.

Sample No	Photo-Conductivity (1/(Ω.cm))	Dark-Conductivity (1/(Ω.cm))	PC/DC	Activation Energy (eV)	Urbach Energy (meV)	Midgap Abs. (cm^{-1})	E04 (eV)	Tauc (eV)
8903 Non-CA	5.77E-5	1.36E-10	4.23E5	0.78	45	0.5	1.91	1.72
8988 CA	4.56E-5	1.02E-10	4.47E5	0.78	42	0.25	1.91	1.74

From Table 4.5, we can see that He Non CA film has comparable properties with He CA films. Stability of the He films is checked by subjecting the films to a one sun illumination. The photoconductivity of the films decreases as the light soaking is going on. The plot of photoconductivity of He films versus light soaking time is shown in Figure 4.6.

It is apparent that He CA film exhibits a smaller degradation rate than He non CA film, which means that chemical annealing technique does improve the stability of the a-Si: H. In the meanwhile, their electrical properties can be very close shown in Table 4.5. However, the differences in film properties are small.

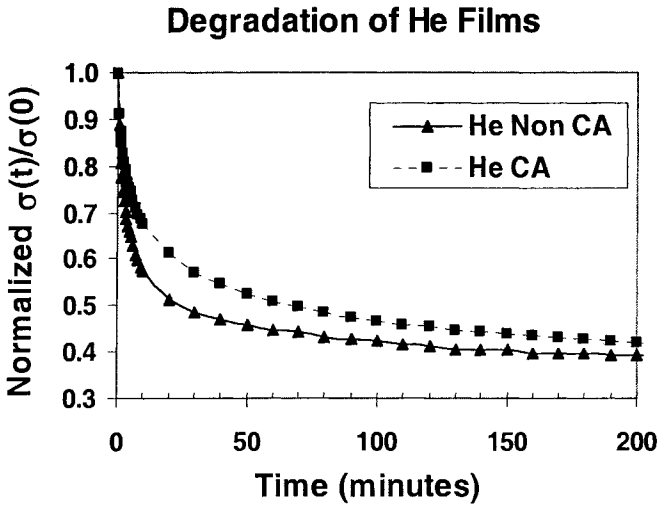

Figure 4.6 Degradation of He films.

4.2 H_2 Plasma Sample

4.2.1 Microstructure information

Films produced using hydrogen plasma annealing was prepared as well. It is found that there is no difference in crystallinity as the annealing time changes. The Raman still shows an amorphous structure even when a 60s annealing time was applied (see Fig. 4.7). The deposition parameters of the H_2 CA films are provided as follows. Table 4.6 gives the X-ray and Raman results for H_2 CA films.

	Temp	Pressure	H_2 (p)	SiH_4 (i)	TMB
Growth time (t1)	340°C	15mT	60%	15%	15%
Anneal time (t2)	340°C	10mT	60%	0%	15%

The Raman data for 8317 which was deposited under an annealing time of 60s is provided in Figure 4.7. From this figure we can see that it is still amorphous structure even when annealing time is 60s. This is quite different from He CA, where a crystalline structure appears when annealing time is more than 10s.

Table 4.6, X-ray and Raman measurements for H_2 CA films

Sample No	Temperature (°C)	Pressure ı (mT)	t1/t2	Thickness (um)	Grain size <111>	Grain size <220>	520cm^{-1}/490cm^{-1} peak ratio
8290	340	15	10s/10s	0.52	N/A	N/A	1
8288	340	15	10s/20s	0.71	N/A	N/A	1
8289	340	15	10s/30s	1.25	N/A	N/A	1
8313	340	15	8s/30s	1.19	N/A	N/A	1
8317	340	15	8s/60s	1.14	N/A	N/A	1

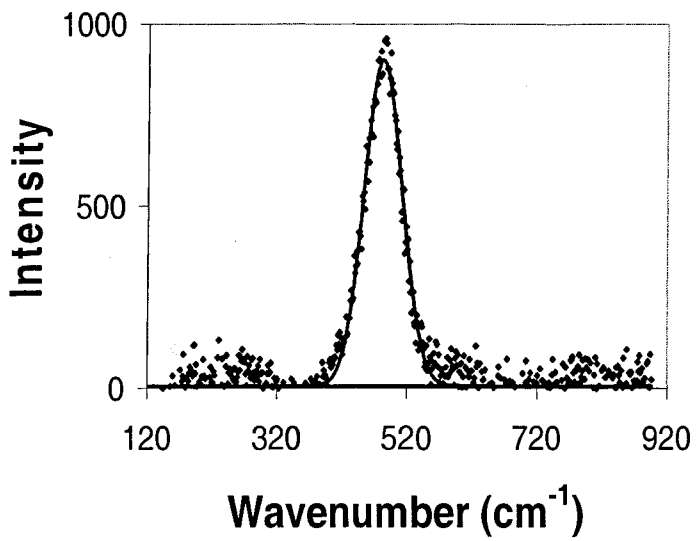

Figure 4.7 Raman spectra for H_2 CA film with an annealing time of 60s.

And the X-ray data for 8317 is shown in Figure 4.8. It can be seen that there is no peak from the sample except one from the steel substrate, which is consistent with the Raman data and tells that 8317 is amorphous structure.

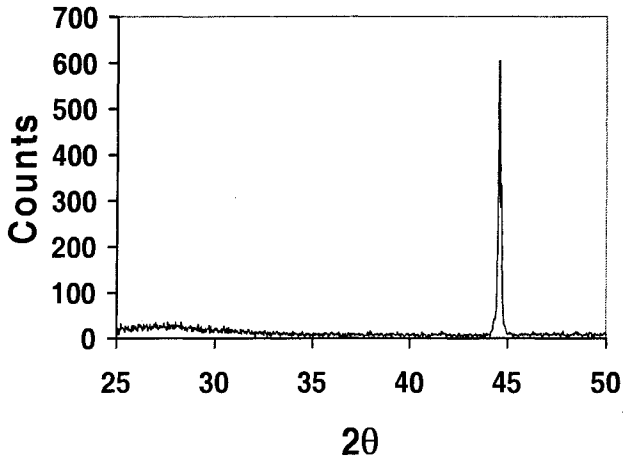

Figure 4.8, X-ray spectra for 8317, the sharp peak at 45°C is from steel substrate.

4.2.2 Electrical properties

The deposition parameters of H_2 CA films and non CA films are provided as follows. And the annealing time is 10s. The parameter of H_2 Non CA is:

Pressure	Temp	H_2 (p)	SiH_4 (i)	ppm TMB
15mT	325°C	60%	15%	25%

And the parameter for H_2 CA is:

	Temp	H_2 (p)	SiH_4 (i)	ppmTMB	H2(i)
Growth time (10s)	325°C	60%	15%	36%	10%
Annealing time (10s)	325°C	60%	0%	36%	10%

As mentioned above, 10% hydrogen from intrinsic line was introduced because this will help flush out the SiH_4 gas during annealing period and decrease the switch time between growth period and annealing period. During the growth period, the pressure is 15mT and it is 13mT for annealing period.

Like He films, stability, conductivity, E_{04}, Tauc energy, activation energy, Urbach energy, and midgap absorption coefficient are measured for H_2 films. Table 4.7 gives the summary of the properties of H_2 non CA films and He CA films.

Table 4.7, properties of He films.

Sample No	Photo-Conductivity (1/(Ω.cm))	Dark-Conductivity (1/(Ω.cm))	PC/DC	Activation Energy (eV)	Urbach Energy (meV)	Midgap Abs. (cm^{-1})	E_{04} (eV)	Tauc (eV)
8904 Non-CA	5.1E-6	4.58E-11	1.11E5	0.77	45	0.5	1.88	1.70
9022 CA	2.7E-6	2.07E-11	1.30E5	0.8	43	0.3	1.85	1.70

H_2 non CA film shows comparable properties with H_2 CA films in Table 4.6. Stability of the H_2 films is checked by subjecting the films to a one sun illumination. The photoconductivity of the films decreases as the light soaking is going on. The plot of photoconductivity of He films versus light soaking time is shown in Figure 4.9.

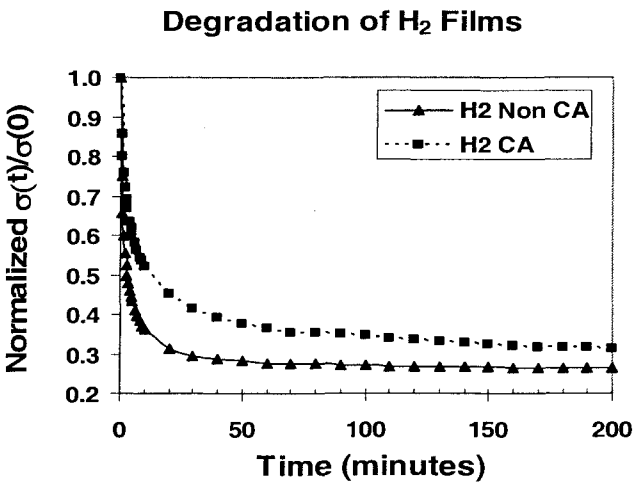

Figure 4.9, Degradation of H_2 films upon light illumination

From Fig. 4.9, it can be seen that H_2 CA film exhibits a smaller degradation rate than H_2 non CA film, and the chemical annealing technique also works for hydrogen films.

CHAPTER 5 DEVICES RESULTS

5.1 He Plasma Devices

5.1.1 He Non CA devices

In order to obtain He Non CA devices with good performance, careful comparison experiments were developed. Among them, the most important factors are: pressure, TMB grading, deposition temperature and hydrogen addition.

Pressure is a very important factor in producing He devices. It is reported that too much ion impinging can actually causes damage to the lattice during growth and this in turn results in a decreased carriers' mobility in solar cells [30]. Since He ion has a higher ion energy than H ion, the pressure for preparing He cells can not be as low as hydrogen cells. Here a comparison experiment is shown. Two samples are deposited in the same parameter except that one is finished at 25mT and another is done at 15mT.

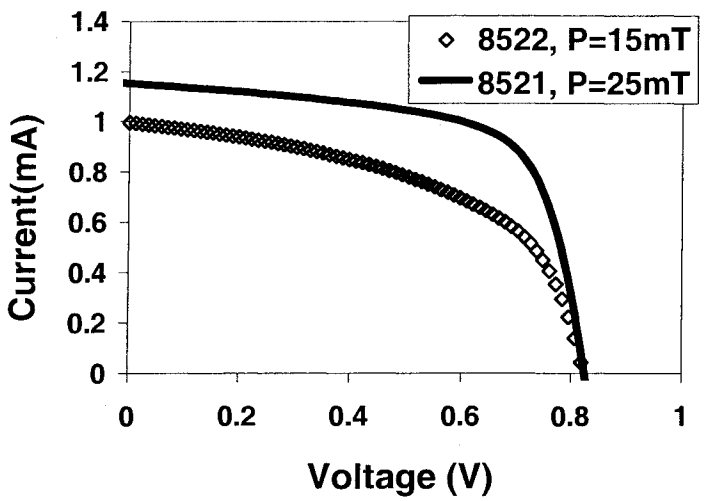

Figure 5.1, pressure effect on the performance of He Non CA cells

From Fig. 5.1, we can see that the sample prepared at 25mT shows a much higher Fill Factor than does the sample prepared at 15mT, which confirms that a too low pressure does harm to the cells' performance.

Hydrogen is reported to play a very important role in producing a-Si:H when inert gas such as Ar or He is used as plasma gas[30]. It is thought that it is necessary to have both H and Ar present to prepare good a-Si:H films. This observation is explained by Ar or He breaking the surface bonds, and H playing a role in enhancing radical selectivity, and surface homogenization and reconfiguration of the subsurface bonds during growth. Therefore, it can be thought that Ar or He plasma dissociate silane efficiently, giving high growth rates, and Ar (or He) and H ions play a role in improving the growth chemistry. Two comparison samples are prepared. All the parameters are the same for these two devices except the amount of the hydrogen which is introduced from plasma line of the PE CVD system.

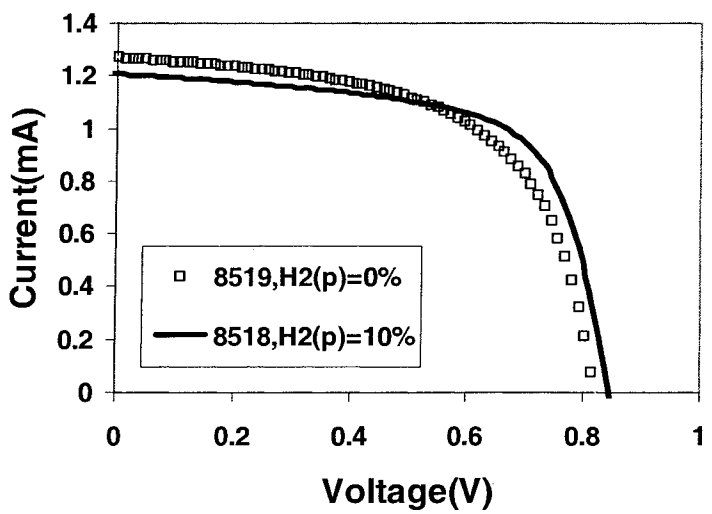

Figure 5.2, I-V curves corresponding to different hydrogen flow rate

It is apparent that when 10% hydrogen is introduced, the Voc increased a little which result in a little bit decrease of short circuit current. However, the FF factor of this sample is much higher (65%) than that of the sample deposited without hydrogen present (FF=59%).

We know that a graded ppm TMB is very important in order to obtain good devices. A graded ppm TMB is thought to introduce an internal electric field in i layer which in turn helps the transportation of the carriers (holes and electrons). Figure 5.3 (a) gives the band diagram of an a-Si:H solar cell with graded i layer. Three comparison samples are prepared: 8507, 8509, and 8510. 8507 has no TMB grading; 8509 has a grading step of 5 minutes; and 8510 has a grading step of 3 minutes. Their total thicknesses are very close and their FF versus the grading step is plot in Figure 5.3(b).

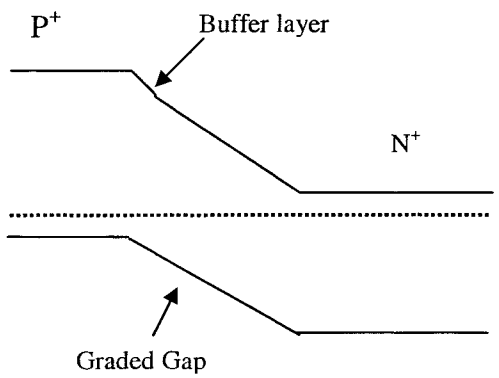

Figure 5.3 (a) Schematic diagram of graded gap cell

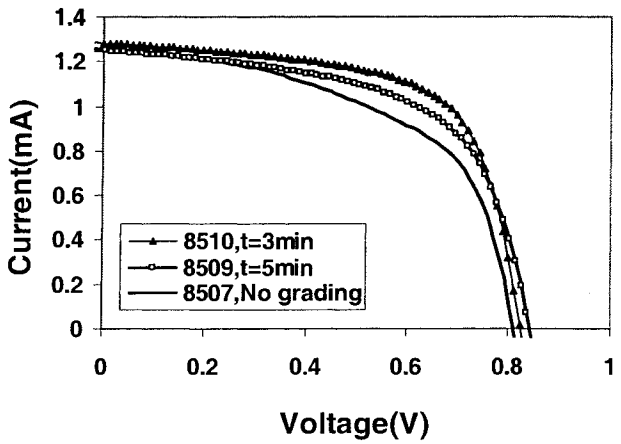

Figure 5.3 (b) I-V curves corresponding to different TMB grading

The single layer without TMB grading has a FF of 55%, and a step of 5min TMB grading gives a FF of 59%. When a step of 3min is applied, the FF increases to 65%. Therefore, it can be seen that a fine TMB grading does improve the devices' performance significantly.

It is well know that low temperature normally gives a better sample than high temperature, because in low temperature, fewer H-bonds are broken. However, devices finished at high temperature have a better stability than low temperature sample. The reason is that in high temperature, radicals leading to film growth are more mobile, and hence results in a denser microstructure which leads to a more stable film. In order to obtain a high stability, therefore materials deposited at a high temperature (315°C-365°C) are preferred, which are more stable, with a lower saturated state density than the lower-temperature-growth materials [17].

Based on those concerns stated as above, a pressure of 25mT, a substrate temperature of 365°C, a graded ppm TMB with a step of 2min, and 10% hydrogen from plasma line are

applied. A He non CA device with good performances is obtained. I-V curve of this sample is provided in Figure 5.4 and the sample number is 8524. The detailed parameter is provided as follows.

Temp	He (p)	H_2 (p)	SiH_4 (i)	ppm TMB
365°C	50%	10%	10%	0-30%

The FF of this sample is 65%, the short circuit current is 1.18mA, and open circuit is 0.82 V. These properties clearly show the characteristics of typical a-Si:H solar cells.

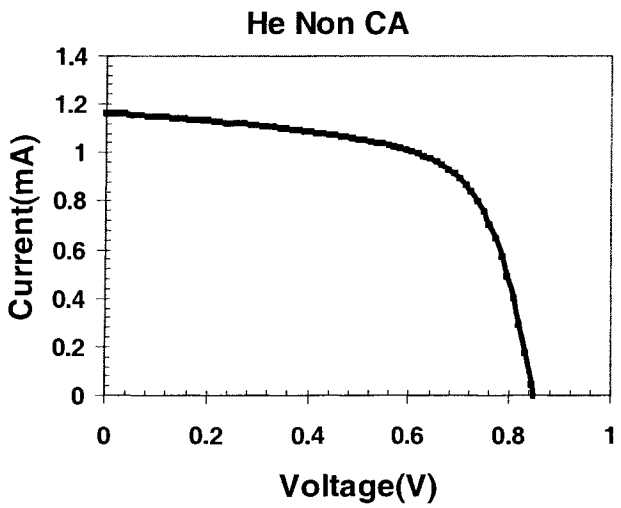

Figure 5.4, I-V for 8524, a He non CA device

5.1.2 He CA devices

Nanocrystalline He CA devices

As mentioned in the 4.1.1, when annealing time is more than 10s, a nanocrystalline structure is obtained. In order to confirm that the nanocrystalline films produced using He annealing were of electronic properties, a p-i-n device is made, and the i2 layer has the similar deposition parameter as He CA nc-Si films. The parameter is provided here.

	Temp	He (p)	SiH_4 (i)	ppm TMB	H2 (i)
Growth time (10s)	365°C	25%	15%	0-28%	10%
Annealing time (20s)	365°C	25%	0%	0-28%	0%

The results of the illuminated I-V curve are shown in Figure 5.5. They clearly show the characteristic voltage (~0.5V) typical of nanocrystalline Si:H cells. The QE data shown in Figure 5.6 confirm that the cells are nanocrystalline since the QE is going out to 800nm.

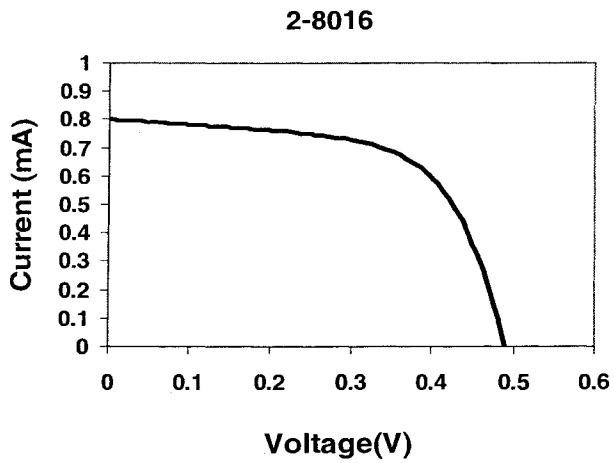

Figure 5.5 Device I-V curve. Voltage of 0.5V indicative of nanocrystalline Si:H

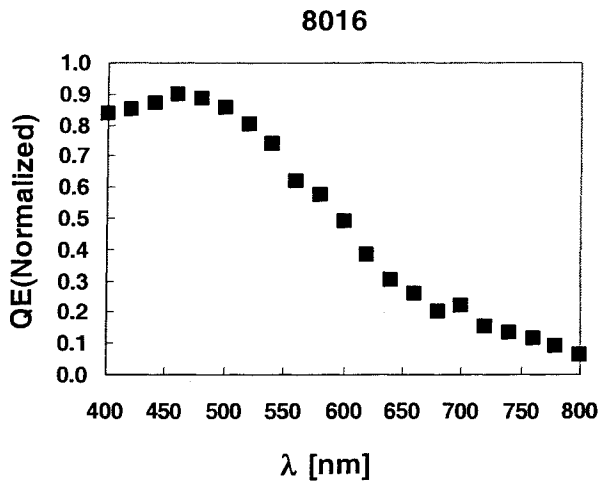

Figure 5.6 QE of He CA nanocrystalline device.

Amorphous He CA devices

The a-Si:H CA device was made based on the parameters from good a-Si:H non CA device 8524. The idea is to divide the i2 layer of a-Si:H non CA device into a number of small layers and each layer is followed by a helium ion impinging treatment. Thus the chemical annealing process is called layer by layer technique. The working He CA device is 8630 and the parameter of i2 layer is provided as follows.

	Temp	He(p)	H_2(p)	SiH_4(i)	ppmTMB	H_2(i)
Growth time (10s)	365°C	50%	10%	10%	7-49%	5%
Annealing time (10s)	365°C	50%	10%	5%	7-49%	5%

The total cycle (10s growth plus 10s annealing is considered as one cycle) number is 70, and the TMB grading step is every 10 cycles. Before the CA layer, there is a 7 minutes' incubation layer, and after the CA layer, there is a layer of 8 minutes' transition layer for i1. 10% hydrogen from plasma line is used to improve the quality of the a-Si:H, and 5% hydrogen from intrinsic line is introduced to flush out the silane in the annealing period and obtain a faster switch time between growth period and annealing period. 5% SiH_4 other than 0% is used in annealing period because it is found that when 0% SiH_4 was applied both the current and the FF were poor. This probably due to the too much ion bombardment of He plasma. I-V curve of this sample is shown in Fig. 5.7, and the FF is 66%.

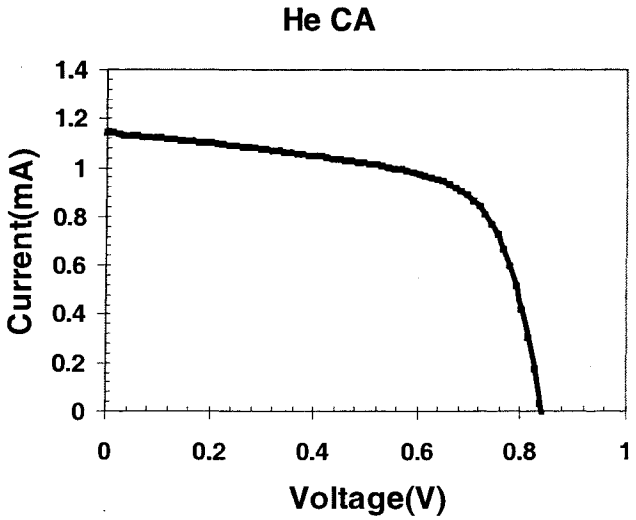

Figure 5.7, I-V curve for 8630, a He CA device.

We know that in order to check the stability difference between He non CA sample and He CA sample, the CA sample and non CA sample must be identical in everything (p+, n+, i1, i2 thickness) except the i2 layer. Their properties are provided in Table 5.1, and it can be seen that they possess very similar properties even in I_{sc}, V_{oc}, FF and QE.

Table 5.1 Properties of He CA and non CA devices.

Sample No	FF(%)	V_{oc}(V)	I_{sc}(mA)	thickness (um)
8524(non CA)	65	0.85	1.16	0.25
8630 (CA)	66	0.84	1.14	0.25

The QE for He non CA (8524) and CA (8630) are also provided in Figure 5.8, where they exhibit very close performances.

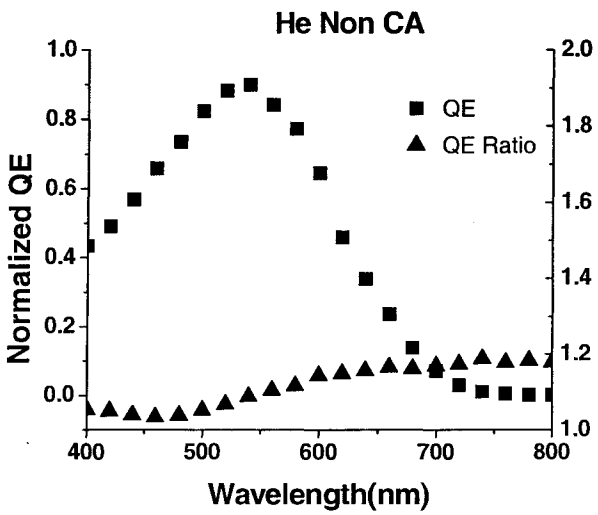

Figure 5.8 A, QE for He non CA sample (8524)

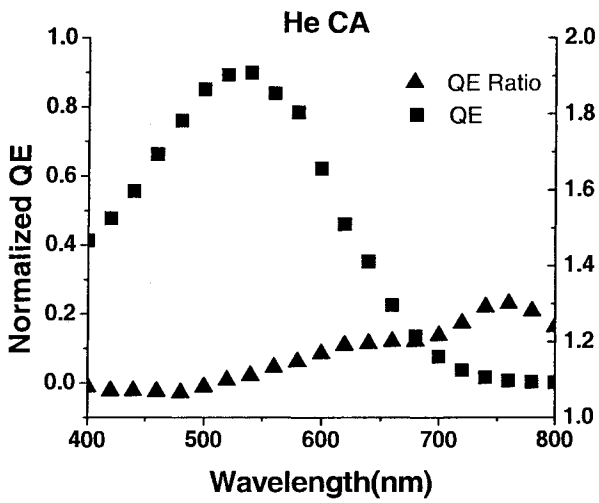

Figure 5.8 B QE for He CA sample (8630)

5.1.3 Stability measurements

The stability of devices was measured using an ELH lamp whose intensity was adjusted to 200mW/cm^2 with the films and devices being kept close to 300°K.

Two identical devices mentioned above, He non CA (8524) and He CA (8630), were subjected to the light illumination for more than 70 hours. The gradation of the FF versus light soaking time is plotted in Figure 5.9. The error in data is about 2%.

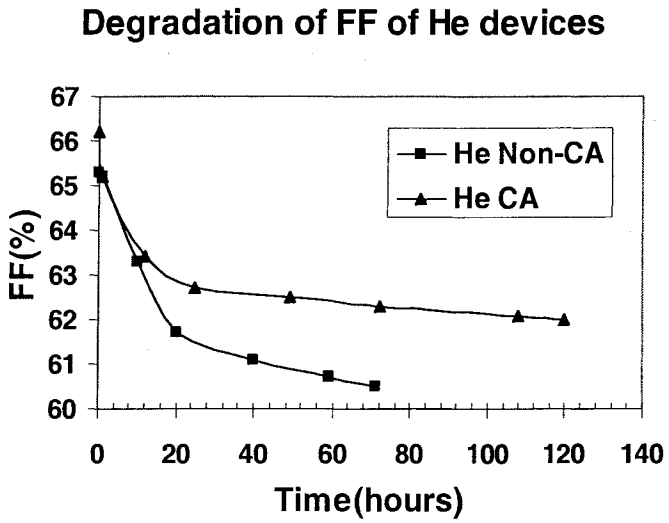

Figure 5.9, Degradation in fill factor of the non-annealed and annealed cells

In Fig.5.10, we show the data on H bonding in films deposited on Si wafers. Fig.5.10 (A) refers to the film which was produced without any chemical annealing (continuous growth). It is seen that there is a significant SiH_2 type bonding in this film. Fig. 5.10 (B) shows the data for a film produced using a chemical annealing with He. It is clearly seen that using a chemical annealing with He significantly reduces the SiH_2 content of the film and also reduces the H content. The relative proportion of SiH_2 bond with respect to the total bonded hydrogen can be defined $R=I_{2080}/(I_{2000}+I_{2080})$, R means the ratio of the measure the integrated intensity I_{2080} of the stretching band centered around 2080cm^{-1} to that of the whole stretching vibration band $I_{2000}+I_{2080}$, (i.e. the bands at 2080 and 2000cm^{-1}). In the non CA case, R=0.27, and R=0.04 for the CA case. The hydrogen content is also calculated from the

integrated intensity of the wagging band centered at 640cm^{-1}.It is found that CA sample has a hydrogen content of 14% while it is 19% for He non CA film.

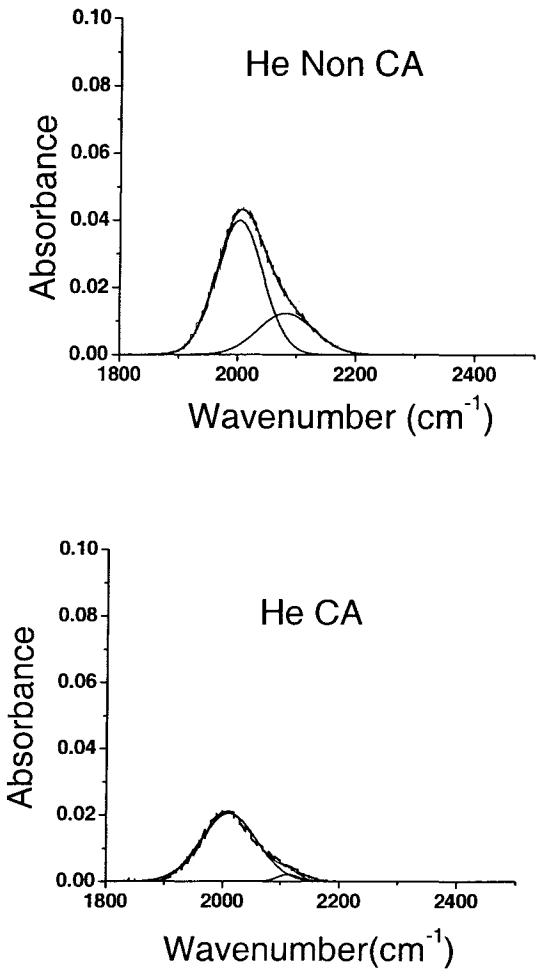

Figure 5.10, FTIR data for He non CA film (upper) and CA film (bottom)

Properties of the non CA and CA devices are studied. Figure 5.11 shows the QE ratio both for non CA cell and CA cell. Upon comparing the two cases, the ratio in long wavelength QE, which is due to holes, is less for chemical annealed case than for the non annealed case. We know that a higher the QE ratio translates into a poorer $\mu\tau$ product which

leads to a worse FF. And this result matches the fact that after light soaking the He CA sample gives a less degradation than He non CA.

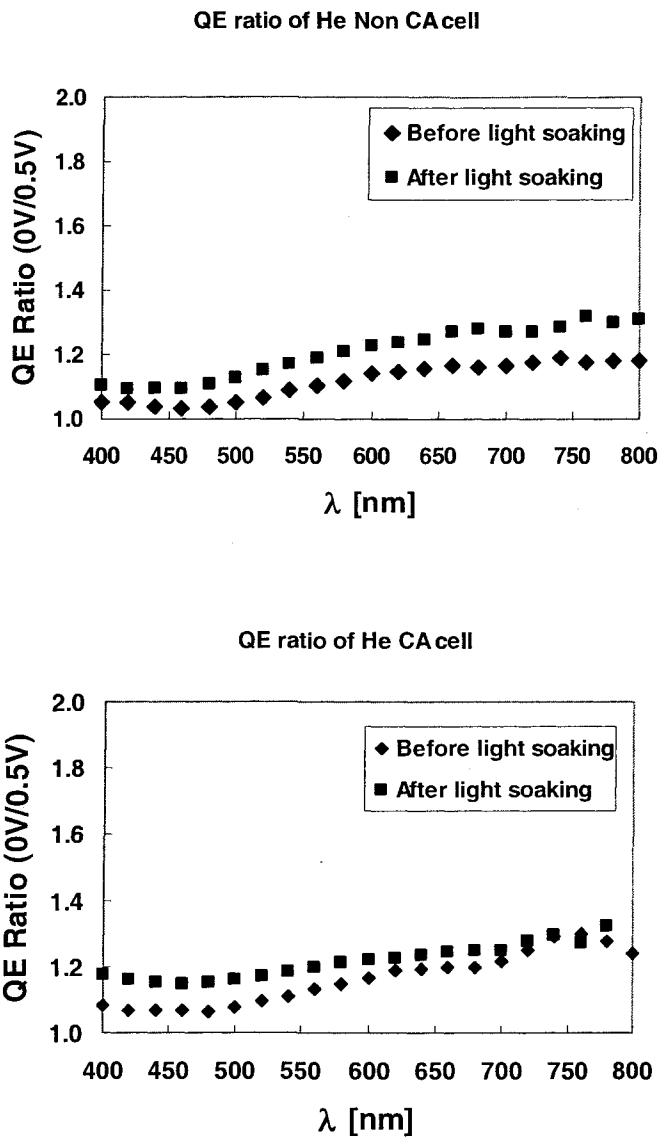

Figure 5.11 Quantum efficiency ratio vs. wavelength for non-annealed and annealed devices, before and after degradation. Note the small change in long wavelength QE ratio for the annealed film compared to non CA devices. This indicates that holes are being collected relatively efficiently even after degradation. In the short wavelength, QE ratio increases after light soaking, and this indicates a deteriorated p-i interface.

The Urbach energies of He Non CA and CA devices before and after light soaking were checked as well. It is found that the midgap absorption increases after light soaking in both cases, which indicates an increased defect density and corresponds to the degradation of the FF. However, the Urbach energy doesn't change after light soaking. The Urbach energy values are shown in Table 5.2 and the subgap measurement of He CA is provided in Figure 5.12.

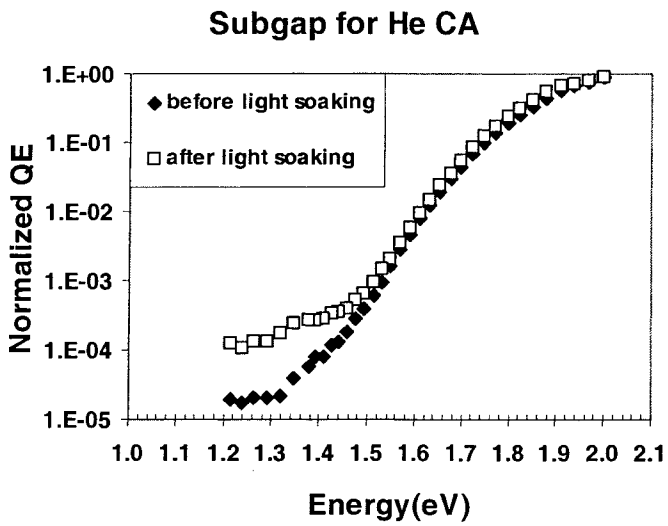

Figure 5.12 Subgap of He CA cell before and after light soaking

Another important factor to indicate the properties of the solar cell is minority holes' mobility-lifetime ($\mu\tau$) product. A higher ($\mu\tau$) properties means a better qualities of the a-Si:H layer. One of the measurement of He Non CA before light soaking is shown in Figure 5.13. It is found that both for He CA (8630) and He non CA (8524), the $\mu\tau$ product increases after the light soaking. This matches the degradation of the FF. The summary about the $\mu\tau$ product is provided in Table 5.2. The summary of the properties of He non CA and CA cells is shown in Table 5.2.

Table 5.2, Properties summary of He cells.

Sample No.	E_{ur} (Before Light Soaking)	E_{ur} (after Light Soaking)	$\mu\tau$ (Before Light Soaking)	$\mu\tau$ (after Light Soaking)	C_H (%)
8524 (He non CA, 365°C)	40	40	1.20E-8	9.10E-9	15
8630 (He CA, 365°C)	42	43	1.16E-8	1.06E-8	14.5
8917 (He CA, 265°C)	42	42	2.10E-8	9.00E-9	17.8

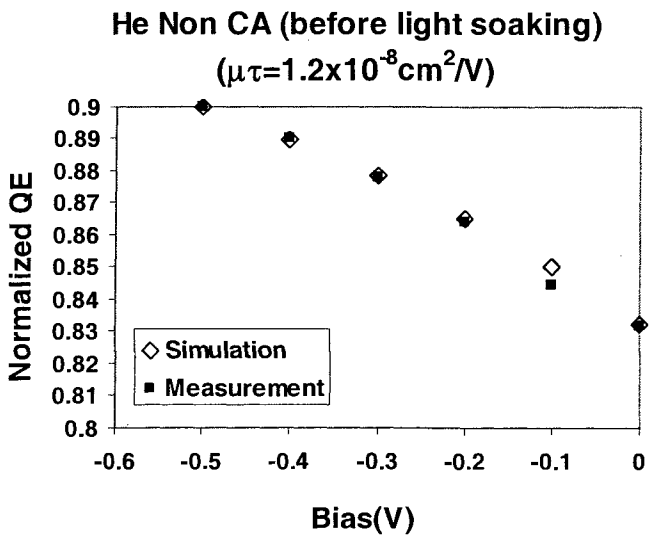

Figure 5.13 $\mu\tau$ product of the He Non CA cell before light soaking

In Table 5.2, another He CA sample (8917) is listed. It has the same deposition parameters as 8630 except that 8917 is prepared at 265°C. The stability comparison between 8630 (365°C) and 8917 (265°C) was carried out. Shown in Figure 5.14, a significant difference takes place and the He CA cell deposited at 365°C performs worse initial FF but a much better stability than that prepared at 265°C. Therefore, this proves that a higher temperature typically gives worse initial properties but a better stability than lower temperature. The stability measurement results are shown in Figure 5.14.

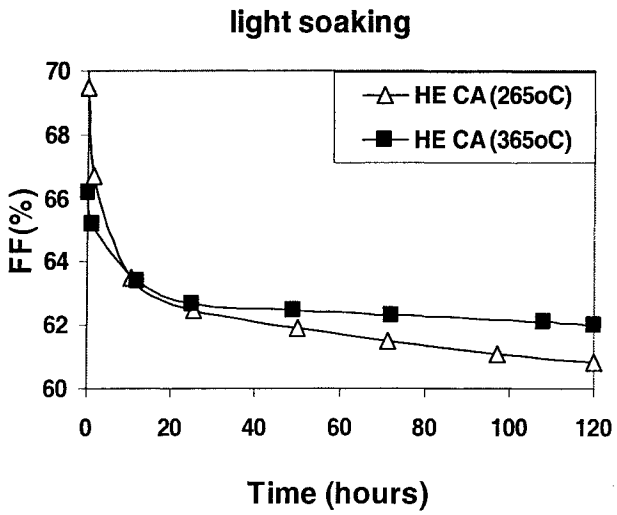

Figure 5.14, stability of He CA cells at different substrate temperature.

FTIR data corresponding to the devices are shown in Figure 5.15. It can be seen that 365°C deposition temperature introduces a much smaller SiH_2 ratio than 265°C does. This matches the theory that a higher temperature introduces less SiH_2 content, and the SiH_2 density is closely related with the stability.

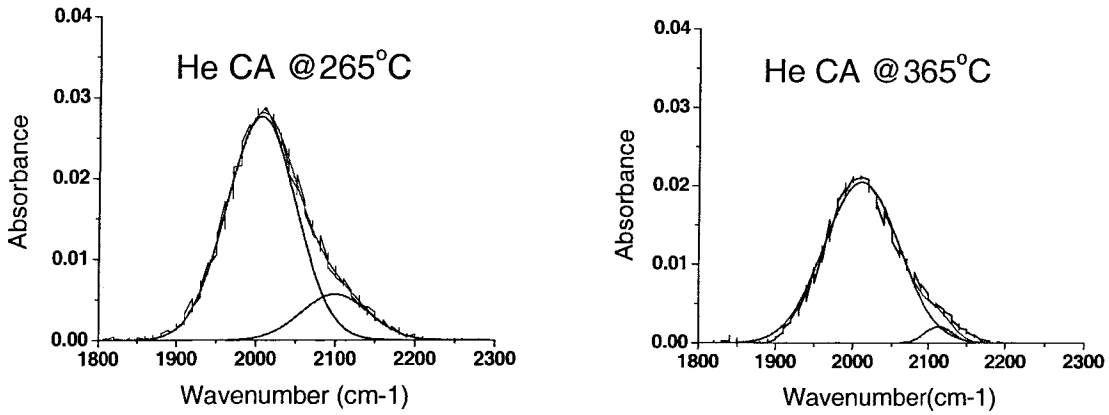

Figure 5.15, FTIR data for He CA films deposited at 265°C and 365°C respectively.

From the data, it is clear that chemical annealing (CA) using helium leads to significant improvements in hydrogen microstructure. The ratio of SiH_2 to SiH bonds decreases significantly under otherwise identical conditions. The data on films (Figure 4.5) produced using CA showed that the degradation in photoconductivity of films was much less than the degradation of photoconductivity in non-CA films. From the data on devices, it is clear that the CA devices also behave very similarly; they degrade much less than the non-CA devices. Unlike previous work [35], both sets of devices in our case had reasonably high fill factors, and the quantum efficiency data, Urbach energy and $\mu\tau$ product showed that the material quality was reasonably good in both cases initially, with only a small decrease in long wavelength QE when the device was subjected to forward bias. After light soaking, the CA device showed significantly less degradation than the non-CA device, and the corresponding QE ratio curves also indicated a better material quality after degradation in the CA device compared to the non-CA device. The $\mu\tau$ product measurements exhibited deteriorated values after light soaking both for the He non CA and CA devices, which is corresponding to the degraded FF. From these results, we conclude that chemical annealing with an inert gas, helium, indeed, results in a significant improvement in hydrogen microstructure, and in the stability of both films and devices in a-Si:H. Note that too much annealing results in the film becoming nanocrystalline, an extreme case of ordering in amorphous materials.

5.2 H_2 plasma Devices

5.2.1 H_2 non CA devices

A regular H_2 non CA device (8662) was prepared with a graded TMB i2 layer and a deposition temperature of 365°C. I-V curve of this sample is shown in Figure 5.16.

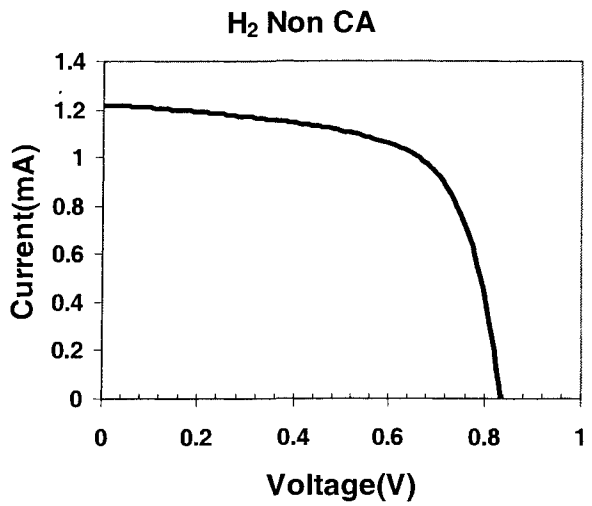

Figure 5.16, I-V curve for H_2 non CA device

In addition, two more similar H_2 non CA devices are produced. One (8850) has a same graded TMB i2 layer as 8662 except that deposition temperature is 265°C, the other (8841) is also prepared at 265°C but i2 layer is not graded with TMB. Table 5.3 summarized the characteristics of these three devices.

Table 5.3 Properties of H_2 non CA devices.

Sample No	Temp(°C)	FF(%)	V_{oc}(V)	I_{sc}(mA)	Thickness (um)
8662 (graded)	365	66	0.84	1.23	0.25
8850 (graded)	265	69	0.84	1.2	0.25
8841 (non-graded)	265	69	0.86	1.3	0.25

Apparently, 265°C gives better initial properties for the H_2 non CA devices because of the higher H content and less dangling bond density.

5.2.2 H_2 CA devices

H_2 CA device is produced based on the working H_2 non CA device (8662). Like the procedures to prepare He CA device, the i2 layer of H_2 non CA device is divided into a number of small layers, and each layer is followed a H ion bombardment layer. The typical parameter of a H_2 CA device is shown as follows.

	Temp	H_2(p)	SiH_4(i)	ppmTMB	H_2(i)
Growth time (10s)	365°C	60%	15%	0-76%	10%
Annealing time (10s)	365°C	60%	0%	0-76%	10%

The total cycle (10s growth plus 10s annealing is considered as one cycle) number is 100, and the TMB is graded by every 5 cycles. Before the CA layer, there is a layer of 10 minutes' incubation layer, and after the CA layer, there is a layer of 10 minutes' transition layer for i1. 10% hydrogen from intrinsic line is introduced to flush out the silane in the annealing period and obtain a faster switch time between growth period and annealing period. Different from He CA sample, there is no SiH_4 during the annealing period, because it is found that if silane was introduced in annealing period, the stability became worse, and this will be discussed in the following section.

A good sample with a FF of 65% is picked up for light soaking. I-V curve of this sample is shown in Fig. 5.17, and the sample number is 8899.

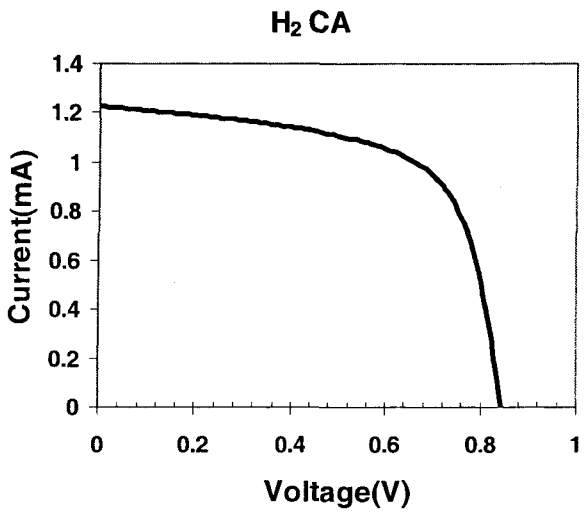

Figure 5.17, I-V curve of H_2 CA device.

This H_2 CA device has comparable initial properties compared with the H_2 non CA device 8662. Table 5.4 gives the comparison.

Table 5.4, comparison between H_2 CA device and H_2 non CA device

Sample No	Temp(°C)	FF(%)	V_{oc}(V)	I_{sc}(mA)	Thickness (um)
8662 (H_2 non-CA)	365	66	0.84	1.2	0.25
8899 (H_2 CA)	365	65	0.84	1.2	0.25

Additionally, two more H_2 CA devices are produced to check the stability. One (8768) was introduced 8% SiH_4 during annealing period and the other (8775) has 6% SiH_4 during annealing period. Table 5.5 shows the properties of these three samples.

The stability measurement was developed for three H_2 CA devices and three H_2 non CA devices.

Table 5.5, initial properties of there H_2 CA devices

Sample No	Temp(°C)	SiH_4 introduced in annealing period	FF(%)	V_{oc}(V)	I_{sc}(mA)	Thickness
8899	365	0%	65	0.84	1.2	0.25
8775	365	6%	65	0.85	1.13	0.25
8768	365	8%	66	0.84	1.23	0.25

5.2.3 Stability measurement

Two identical devices mentioned in Table 5.4, H_2 non CA (8662) and H_2 CA (8899) were subjected to 2×sun light illumination for more than 70 hours. The gradation of the FF versus light soaking time is plotted in Figure 5.18. The error in data is about 2%.

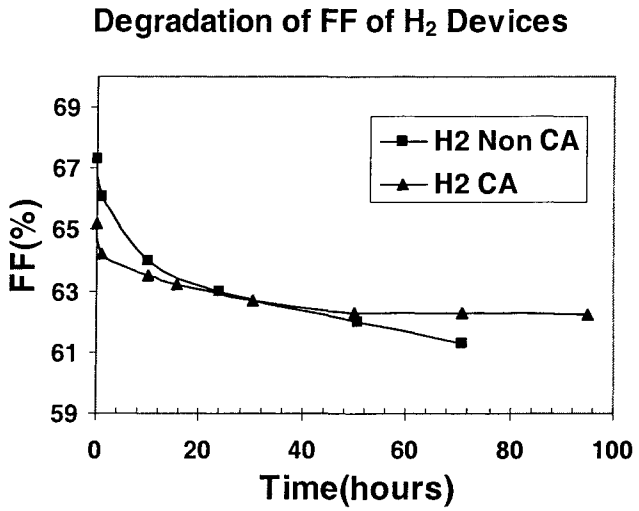

Figure 5.18, light soaking data for H_2 non CA (8662) and H_2 CA (8899)

Apparently, chemical annealed sample possess a much higher stability than non chemical annealed sample. After 71 hours light soaking, the FF of H_2 non CA (8662) sample dropt from 67% to 61%, while the H_2 CA (8899) sample's FF is still 63% after 95 hours light

soaking. This result is consistent with the light soaking data from films in Figure 4.8, where H_2 CA film also performs a better stability than H_2 non CA film.

Figure 5.19 gives the FTIR data of H_2 CA film and H_2 non CA film in silicon wafer.

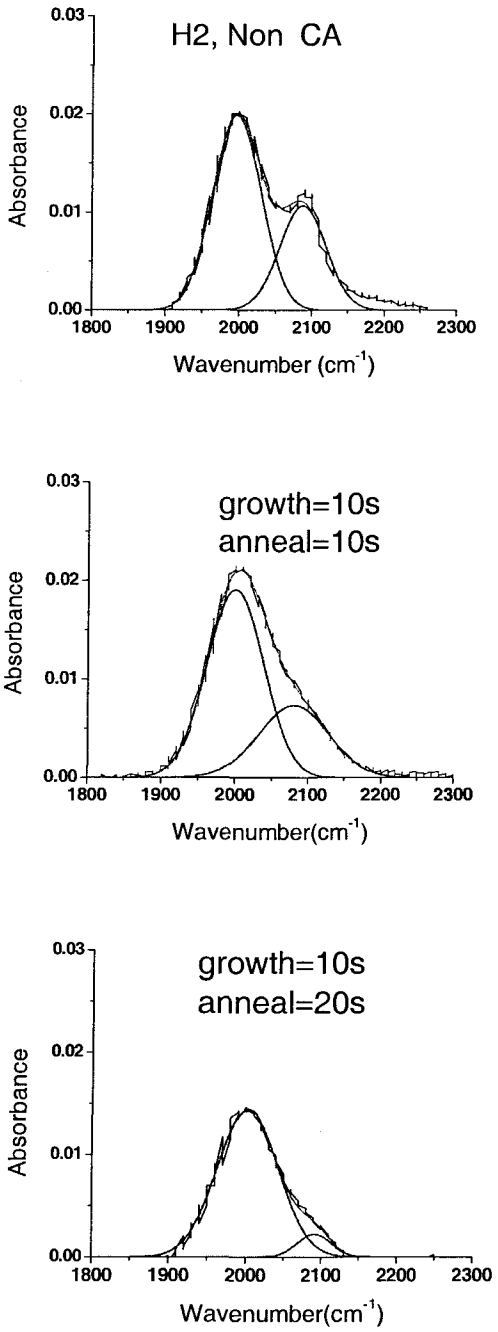

Figure 5.19, FTIR data of the H_2 CA and non CA films

Figure 5.19 clearly shows the significant decrease of SiH_2 bond content after chemical annealing treatment. Moreover, the SiH_2 bond content decreases with the increase of the annealing time. This remarkable result indicts the close relationship between SiH_2 bond content and stability of a-Si:H. It also reveals that the chemical annealing does improve the stability of a-Si:H by decreasing the SiH_2 bond content.

After light soaking, it is found that the $\mu\tau$ product was reduced, and the Urbach energy doesn't change, but the midgap absorption increased. The summary of these data are shown in Table 5.6. Figure 5.20 shows the subgap measurement of H_2 CA sample. Clearly, it can be seen from Fig. 5.20 that after the light soaking the midgap absorption increases and this is corresponding to the degradation of the FF in I-V curve.

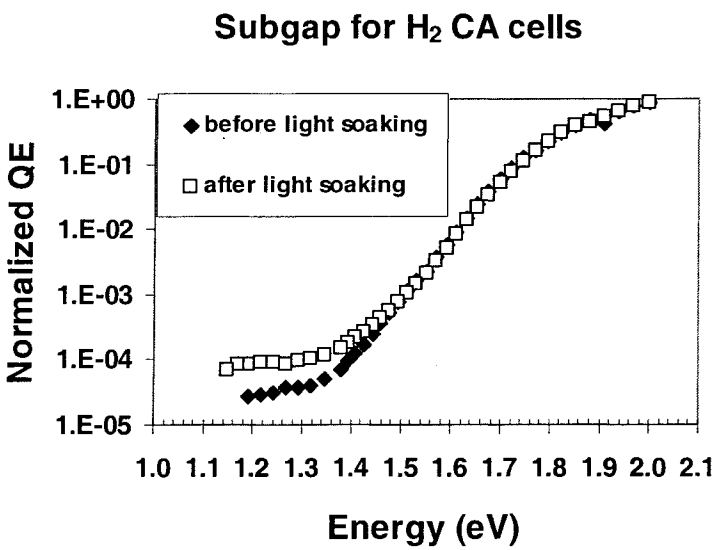

Figure 5.20 Subgap measurements of H_2 CA devices.

The QE ratios of both samples are measured and shown in Fig. 5.21. It is found that the QE ratio of H_2 non CA sample increased a lot, while that of the H_2 CA sample has very

small change. This is very consistent with the stability data, which shows that H_2 CA sample has much smaller degradation than H_2 non CA cell.

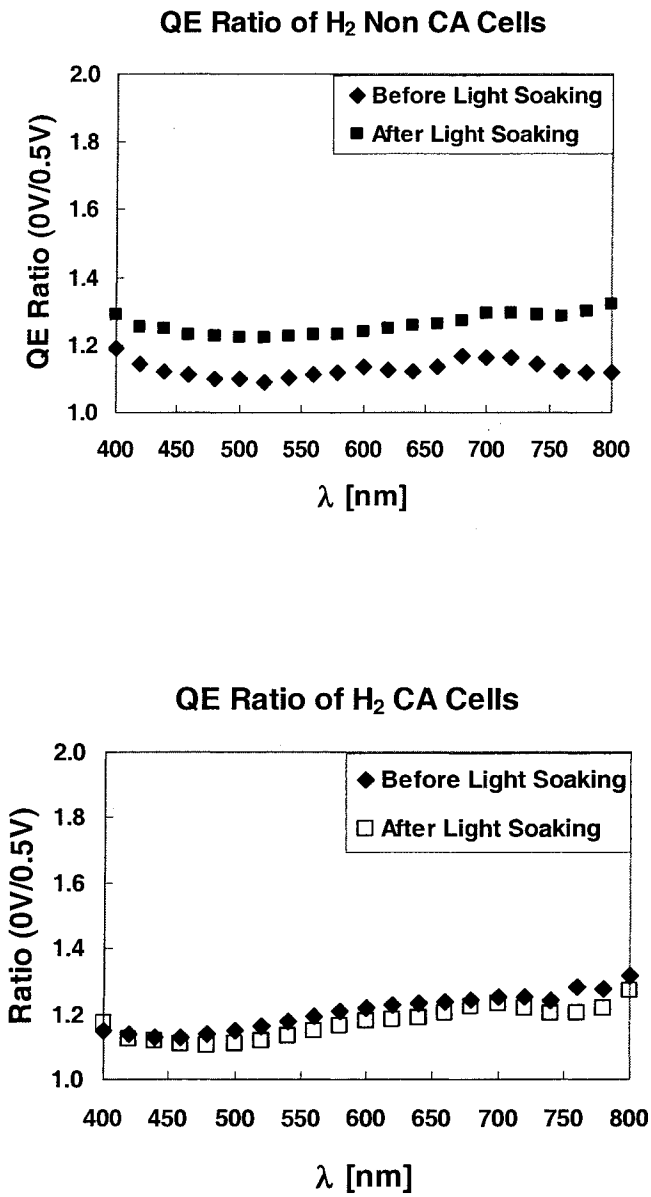

Figure 5.21 QE ratio data of H_2 CA and non CA cells

Stability comparison in three H_2 CA devices mentioned in Table 5.5 is also checked and shown in Figure 5.22. In Figure 5.22, "SiH_4=15%/8%" means that 15% SiH_4 was introduced in growth period and 8% SiH_4 was introduced in annealing period in each cycle. It can be seen in Figure 5.22 that the less the SiH_4 was introduced in the annealing period, the better the stability was exhibited in the stability measurements. It can be understood in this way. If less silane is introduced in the annealing period, this improves both the etching and the bombardment of hydrogen plasma, and thus can reduce the weekly Si-Si and Si-H bonds more significantly. Corresponding, the stability of the device is improved.

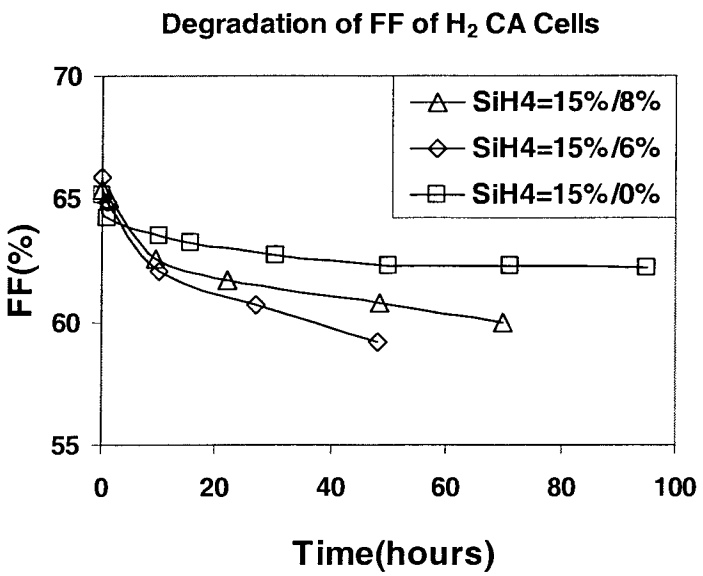

Figure 5.22, degradation of H_2 CA devices with different SiH_4 in annealing period.

Light soaking experiment data for three non-chemical annealed H_2 cells listed in Table 5.3 were provided in Figure 5.23. Clearly, sample finished at high temperature (365°C) shows better stability than sample prepared at low temperature (265°C), and sample with a graded TMB i2 layer possesses a better stability than that with a non-graded TMB i2 layer. A

graded TMB i2 layer is assumed to introduce an internal electric field and this in turn improves the transportation of the carriers in the i2 layer and thus increases the FF.

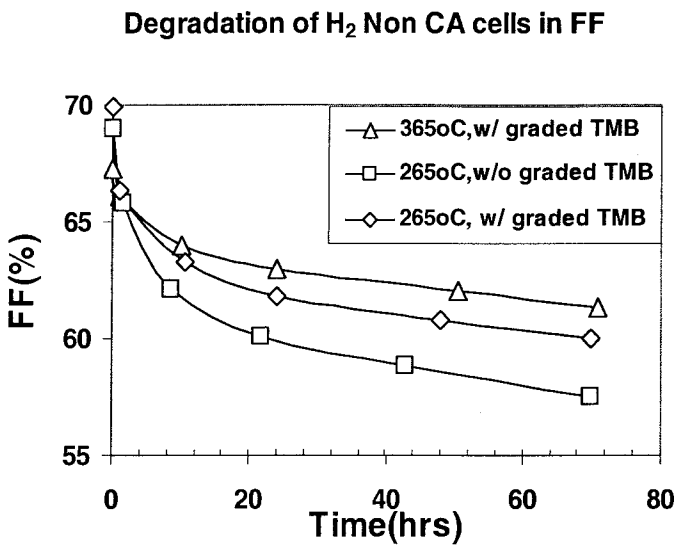

Figure 5.23 Stability of three H_2 non CA cells

Table 5.6 gives the summary of Urbach energy, $\mu\tau$ product, and H content measurement. From all the data mentioned above, it is found that H plasma chemical annealing can significantly reduce the SiH_2 bond content and improve the stability of a-Si:H solar cells. In order to obtain enough etching and bombardment abilities of H plasma, a high hydrogen dilution in annealing period is require. It is found that the stability of H_2 CA devices increase with the decease of SiH_4 flow rate in the annealing period. It is also revealed that device deposited at lower temperature typically obtain a higher SiH_2 bond content and better initial performances than that deposited at higher temperature, but upon light soaking, the former shows a worse stability. Moreover, a graded TMB structure is proved to improve the stability of the devices. $\mu\tau$ product measurements show decreased values after light soaking, which is consistent with the degradation of the FF in devices.

Table 5.6, characteristics of the H_2 cells before and after light soaking

Sample No.	E_{ur} (before light soaking)	E_{ur} (after light soaking)	$\mu\tau$ (before light soaking)	$\mu\tau$ (after light soaking)	C_H (%)
8662 (H2 non CA, 365°C)	42	43	1.51e-8	9.10e-9	16
8850 (H2 non CA, 265°C)	43	43	2.90e-8	7.02e-9	17.2
8899 (H2 CA, 365°C)	41	43	1.48e-8	1.10e-8	15

CHAPTER 6 CONCLUSIONS

In summary, a systematic and careful study has been carried out of the growth and properties of a-Si:H films and devices based on chemical annealing and non chemical annealing techniques. The films and devices were grown using a remote, low pressure ECR plasma process. The following significant results were obtained:

(1) It is found that the structure of the films grown using the layer-by-layer technique depended critically upon whether the annealing was done with hydrogen or helium, and the time taken to do the annealing. When the annealing was done in hydrogen plasma, the films remained amorphous no matter how long the annealing time was; in contrast, when the annealing was done in helium, and the annealing time was more than 10 seconds, the films became crystalline. Moreover, the crystallinity increases as the annealing time increases.

(2) The phenomena that helium plasma annealing converted the amorphous silicon into crystalline contradict the generally accepted assumption that high hydrogen dilutions are needed to crystallize the amorphous films based on the reactive etching of H ions. The result obtained in this work shows that it is not necessary to have a high hydrogen dilution to obtain crystalline films. Rather, the amount of hydrogen already present in an amorphous film is enough to cause crystallization, provided that enough ion flux and perhaps energy are available for converting the amorphous structure to a crystalline structure. This remarkable result suggests that not only the reactive etching effect from the H ions, but also the ion bombardment play a role in crystallizing the amorphous films when high hydrogen dilution is used.

(3) Helium plasma annealed a-Si films and non helium plasma annealed films with comparable initial properties were prepared. Upon light soaking, the chemical annealed a-Si films showed a much lower degradation in photoconductivity than that of non chemical annealed films. Helium plasma annealed a-Si devices and non helium plasma annealed devices with close initial properties were prepared as well. Upon light soaking, the degradation in the most sensitive device factor, the fill factor, showed that chemical annealed devices possessed a much better stability than non chemical annealed devices. FTIR data of chemical annealed films show a much less SiH_2 bond content than that of non chemical annealed films. Clearly, it indicates that chemical annealing technique leads to significant improvement in the stability of both films and devices in a-Si:H by reducing the SiH_2 bond density inside.

(4) In addition, comparable hydrogen plasma annealed a-Si films and non annealed films; comparable chemical annealed a-Si devices and non chemical annealed devices were produced. It was shown that hydrogen plasma annealed films performed lower degradation in photoconductivity than non annealed films. Chemical annealed devices showed a better stability in fill factor than non annealed devices. FTIR data demonstrated that the stability of a-Si:H was closely related to the SiH_2 bond content and the chemical annealing technique did reduce the SiH_2 bond density in a-Si:H greatly.

(5) Comparison data shows that a lower deposition temperature gives better initial properties in devices, a higher SiH_2 bond content in films, and a worse stability upon light soaking than a higher deposition temperature. Also, it is shown that a device with a TMB graded i2 layer obtained a higher stability than that without a TMB graded i2 layer.

(6) It is found that the $\mu\tau$ product of devices reduced after light soaking, which is consistent with the degradation of the FF in devices.

REFERENCES

[1] K.Tanaka, E.Maruyama, et al., Amorphous Silicon, John Wiley & Sons, New York, (1998)

[2] D.L. Staebler and C.R. Wronski, Appl. Phys. Lett., 31 (1977) 292

[3] Donald A. Neamen, "Semiconductor Physics and Devices", 3rd edition, McGraw-Hill, New Delhi, 2003.

[4] S.O. Kasap, Optoelectronics and Photonics: Principles and Practices, Prentice Hall, Upper Saddle River, NJ (2001)

[5] D.J. Wolford, J.A. Reimer, and B.A. Scott, Appl. Phys. Lett., 42, (1983) 369

[6] A. Madan, M.P. Shaw, The Physics an Applications of Amorphous Semiconductors, Academic Press, Inc. San Diego, California (1998)

[7] J.H. Moller, Semiconductors for Solar Cells, Artech House Inc., Boston, MA (1993)

[8] W. Luft and Y. Tsuo, Hydrogenated Amorphous Silicon Alloy Deposition Processes, Marcel Dekker, Inc., New York (1993)

[9] D. Adler, Semiconductors and Semimetals, 21 Academic Press, New York, (1984)

[10] V.L. Dalal et al., Mat. Res. Soc. Symp. Proc. 149 (1989) 601

[11] H. M. Branz, Phys. Rev. B, 59 (8), (1999) 5498

[12] J.B. Dresner, B. Goldstein and D. Szostak, Appl. Phys. Lett., 38 (1981) 998

[13] V.L. Dalal, E. Ping et al., Appl. Phys. Lett., 64 (1994) 1862

[14] V.L. Dalal et al., J. J. of Non-Crystalline Solids, 227-230 (1998) 1257

[15] A. H. Mahan, J. Carapella et al., Appl. Phys. Lett., 64 (1991) 1862

[16] E. Maruyama, S. Tsuda, S. Nakano, Hydrogenated amorphous silicon, Vol. 44-46, Neber-Aeschbacher H. (Ed.), Science Publication, Zurich, Part 2, (1995), 863

[17] V.L. Dalal and Greg Baldwin, Mat. Res. Soc. Symp. Proc., 297 (1993), 833

[18] R.E.I. Schropp, Hydrogenated amorphous silicon, Vol. 44-46, Neber-Aeschbacher H. (Ed.), Science Publication, Zurich, Part 2, 1995, 853-861

[19] S. Guha, in: R. Street (Ed.), Technology and applications of amorphous silicon, Vol.37, Spring, Berlin, (1999) 252.

[20] X. Xu, J. Yang, S. Guha, Thin solid films 198-200 (1996) 60

[21] N. Souffi, A. Matsuda et al., Solid State Commun. 122 (2002) 259

[22] G. Gaungly, A. Matsuda, Phys. Rev. B 49 (1994) 10986

[23] T. Nishimoto, T. Takagi et al., Solar Energy Materials & Solar Cells, 66 (2001) 179

[24] S. Shimizu, H. Miyahara et al., J. of Non-Crystalline Solids, 338-340 (2004) 47

[25] S.M. Pietruszko and J. Jang, Solar Energy Materials & Solar Cells, 71 (2001) 459

[26] J. Yoon, K. Lee, J. of Non-Crystalline Solids, 299-302 (2002) 487

[27] S. Shimizu, M. Kondo, and A. Matsuda, J. Appl. Phys., 97 (2005) 033522

[28] T. Nishimoto, M. Takai et al., J. of Non-Crystalline Solids, 299-302 (2002) 1116

[29] H. Miyahara, M.Takai et al., Solar Energy Materials & Solar Cells, 74 (2002) 351

[30] V.L. Dalal, Thin Solid Films, 395 (2001) 173

[31] A.H Mahan, D.L. Williamson, B.P. Nelson, and R.S. Crandall, Phys. Rev. B, 40 (1989) 12024

[32] V.L. Dalal, G. Baldwin et al., AIP Conference Proceedings, 306 (1994) 460

[33] M. Ito, S. Shimizu et al., J. of Non-Crystalline Solids, 338-340 (2004) 698

[34] G.Q. Pan, X.B. Xiao et al., Chin. J. of Electron, 3 (1994) 80

[35] W. Futako, T. Kamiy, I. Shimizu, J. of Non-Crystalline Solids, 266-269 (2000) 630

[36] H. Sato, K. Fukutani et al., Solar Energy Materials & Solar Cells, 66 (2001) 321

[37] K. Ohkawa, S. Shimizu et al., Solar Energy Materials & Solar Cells, 66 (2001) 297

[38] W. Futako, and I. Shimizu et al., J. of Non-Crystalline Solids, 198-200 (1996) 1046

[39] S. Miyazaki, N. Fukuhara and M. Hirose, J. of Non-Crystalline Solids, 266 (2000), 59

[40] Y. Liu, High growth rate deposition of hydrogenated a-SiGe films and devices using ECR-PECVD (ISU, dissertation, 1995) 17.

[41] S. Matsuo and M. Kiuchi, Low Temperature Deposition Apparatus Using Electron Cyclotron Resonance Plasma, Proc. Symp. VLSI Sci. Technol. Electrochemical Soc., Pennington, NJ, 83 (1983)

[42] S. K. Kaushal, Stability and electronic properties of a-Si p-i-n devices fabricated using ECR plasma enhance chemical deposition, (ISU, dissertation, 1997)

[43] A. Matsuda, M. Koyama, N. Ikushi et al., Japn. J. Appl. Phys. 25 (1986) 54

[44] J. Perrin, M. Shiratani, K. Patrick et al., J. Vac. Sci. Technol. A 16(1) (1998) 278

[45] A. Gallagher, J. Appl. Phys., 63(7) (1988) 2406

[46] V.L. Dalal, R. Knox et al., Conference Record of the IEEE Photovoltaic Specialists Conference, 22^{nd}(2) (1991)1399.

[47] V.L. Dalal, T. Maxson et al., J. of Non-Crystalline Solids, 227-230 (1998) 1257.

[48]S. K. Kaushal, Growth of high Quality a-(Si,Ge):H films using low pressure, remote ECR plasma technique 17, (ISU, thesis, 1995)

[49] D.K. Schroder, Semiconductor Material and Device Characterization, John Wiley & Sons, Inc. New York, (1998)

[50] M. Bermejo, M. Cardona, J. of Non-Crystalline Solids, 32 (1979) 413

[51] B.D. Cullity, Elements of X-ray diffraction, Addison-Wesley Publishing Company, Inc. Boston, MA (1978) 101-102

[52] M. Kondo, S. Yamasaki and A. Matsuda, J. Non-Crystalline Solids, 266-269(2000) 544

[53] D. Zymierska, K. Godwod and J. Auleytner, J. Physics D: Appl. Phys., 36 (2003) A202-A 204

[54] B.W. Faughnan and R. Crandall, Appl. Phys. Lett., 44 (1984) 537

[55] M.H. Brodsky, M. Cardona, and J.J. Cuomo, Phys. Rev. B, 16 (1977) 3556

[56] C.J. Fang, K.J. Gruntz, L.Ley et al., J. of Non-Crystalline Solids, 35&36 (1980) 255

[57] S. Lee, S. Kumar, and C. Wronski, J. of Non-Crystalline Solids, 114 (1989) 316

[58] S. M. Sze, Physics of Semiconductor Device, 2nd Edition, John Wiley & Sons, Inc. New York, (1998)

[59] M. Hack, & M. Shur, J. Appl. Phys., 58 (1985) 997

[60] G. Baldwin, Design and modeling of a graded bandgap amorphous silicon solar cell deposited by plasma enhanced chemical vapor deposition, (ISU, thesis, 1994)

[61] V.L. Dalal, and F. Alvarez, Journal De Physique, Supplement C4, 42 (1981) 491

[62] D.E. Crandall, and C.R. Wronski, Appl. Phys. Lett., 28 (11) (1976) 671

[63] S. Miyazaki, N. Fukuhara, and M. Hirose, J. of Non-Crystalline Solids, 266 (2000) 59

[64] V. L. Dalal, J. Graves and J. Leib, Appl. Phys. Lett., 85 (2004) 1413

ACKNOWLEDGEMENTS

First and foremost, I thank Professor Dalal, my advisor, for his guidance, support and many valuable suggestions. I also want to thank my committee members Dr. Biswas, Dr. Mina, Dr. Shinar, and Dr. Tuttle for serving on my committee and review of my work and for valuable suggestions.

I thank Kay Han and Andy Liu for helping me with sample preparation and research discussions. I am grateful to Max Noack for his technical help and Dr. Ruth Shinar for her suggestions.

In addition, I want to express appreciation for Jason Zhu, Durga Panda, Dan Stieler, Satya Saripalli, Puneet Sharma, Debju Ghosh, Kamal Muthukrishnan, and Vishwas Jaju, for their help and friendship.

I'd like to thank my parents for their support, love and inspirations.

Finally I would like to thank my wife, Yan Li, for her understanding, patience, and love that accompanied me in these years.

The work was supported in part by NREL.